Elsevier Editorial System(tm) for Geochimica et Cosmochimica Acta

Manuscript Draft

Manuscript Number: GCA-D-15-00412R1

Title: Fluid-melt partitioning of sulfur in differentiated arc magmas and the sulfur yield of explosive volcanic eruptions

Article Type: Article

Corresponding Author: Dr. Matteo Masotta, PhD

Corresponding Author's Institution: Universität Bayreuth

First Author: Matteo Masotta, PhD

Order of Authors: Matteo Masotta, PhD; Hans Keppler, Prof.; Alok Chaudhari

Abstract: The fluid-melt partitioning of sulfur (DSfluid/melt) in differentiated arc magmas has been experimentally investigated under oxidizing conditions (Re-ReO2 buffer) from 800 to 950˚C at 200 MPa. The starting glasses ranged in composition from trachyte to rhyolite and were synthesized targeting the composition of the residual melt formed after 10 to 60% crystallization of originally trachy-andesitic, dacitic and rhyodacitic magmas (Masotta and Keppler 2015; Geochimica et Cosmochimica Acta 158, 79-102). Fluid compositions were determined both by mass balance and by Raman spectroscopy of fluid inclusions. DSfluid/melt increases exponentially with increasing melt differentiation, ranging from 2 to 15 in the trachytic melt, from 20 to 100 in the dacitic and rhyodacitic melts and from 100 to 120 in the rhyolitic melt. The variation of the DSfluid/melt is entirely controlled by the compositional variation of the silicate melt, with temperature having at most a minor effect within the range investigated. Experiments from this study were used together with data from the literature to calibrate the following model that allows predicting DSfluid/melt for oxidized arc magmas:

$$\ln(D_S^{fluid/melt}) = 9.2 - 31.4 \cdot nbo/t - 1.8 \cdot ASI - 29.5 \cdot Al\# + 4.2 \cdot Ca\#$$

where nbo/t is the non-bridging oxygen atoms per tetrahedron, ASI is the alumina saturation index, Al# and Ca# are two empirical compositional parameters calculated in molar units ($Al\# = X_{Al2O3}/(X_{SiO2}+X_{TiO2}+X_{Al2O3})$ and $Ca\# = X_{CaO}/(X_{Na2O}+X_{K2O})$).
The interplay between fluid-melt partitioning and anhydrite solubility determines the sulfur distribution among anhydrite, melt and fluid. At increasing melt polymerization, the exponential increase of the partition coefficient and the decrease of anhydrite solubility favor the accumulation of sulfur either in the fluid phase or as anhydrite. On the other hand, the higher anhydrite solubility and lower partition coefficient for less polymerized melts favor the retention of sulfur in the melt. At equilibrium conditions, these effects yield a maximum of the sulfur fraction in the fluid phase for slightly depolymerized melts (nbo/t = 0.05 to 0.15). Our data allow quantitative predictions of the sulfur yield of explosive volcanic eruptions over a wide range of magma compositions.

Fluid-melt partitioning of sulfur in differentiated arc magmas and the sulfur yield of explosive volcanic eruptions

M. Masotta*, H. Keppler, A. Chaudhari

Bayerisches Geoinstitut, Universität Bayreuth, 95440 Bayreuth (Germany)

* Corresponding author
Matteo Masotta
Bayerisches Geoinstitut
Universität Bayreuth
95440 Bayreuth (Germany)
E-mail: matteo.masotta@uni-bayreuth.de
Tel.: +49 (0)921 55 3739

ABSTRACT

The fluid-melt partitioning of sulfur ($D_S^{fluid/melt}$) in differentiated arc magmas has been experimentally investigated under oxidizing conditions (Re-ReO_2 buffer) from 800 to 950°C at 200 MPa. The starting glasses ranged in composition from trachyte to rhyolite and were synthesized targeting the composition of the residual melt formed after 10 to 60% crystallization of originally trachy-andesitic, dacitic and rhyodacitic magmas (Masotta and Keppler 2015; *Geochimica et Cosmochimica Acta* 158, 79-102). Fluid compositions were determined both by mass balance and by Raman spectroscopy of fluid inclusions. $D_S^{fluid/melt}$ increases exponentially with increasing melt differentiation, ranging from 2 to 15 in the trachytic melt, from 20 to 100 in the dacitic and rhyodacitic melts and from 100 to 120 in the rhyolitic melt. The variation of the $D_S^{fluid/melt}$ is entirely controlled by the compositional variation of the silicate melt, with temperature having at most a minor effect within the range investigated. Experiments from this study were used together with data from the literature to calibrate the following model that allows predicting $D_S^{fluid/melt}$ for oxidized arc magmas:

$$\ln\left(D_S^{fluid/melt}\right) = 9.2 - 31.4 \cdot \frac{nbo}{t} - 1.8 \cdot ASI - 29.5 \cdot Al\# + 4.2 \cdot Ca\#$$

where $\frac{nbo}{t}$ is the non-bridging oxygen atoms per tetrahedron, ASI is the alumina saturation index, Al# and Ca# are two empirical compositional parameters calculated in molar units ($Al\# = \frac{X_{Al2O3}}{X_{SiO2}+X_{TiO2}+X_{Al2O3}}$ and $Ca\# = \frac{X_{CaO}}{X_{Na2O}+X_{K2O}}$). The interplay between fluid-melt partitioning and anhydrite solubility determines the sulfur distribution among anhydrite, melt and fluid. At increasing melt polymerization, the exponential increase of the partition coefficient and the decrease of anhydrite solubility favor the accumulation of sulfur either in the fluid phase or as anhydrite. On the other hand, the higher anhydrite solubility and lower partition coefficient for less polymerized melts favor the retention of sulfur in the melt. At equilibrium conditions, these effects yield a maximum of the sulfur fraction in the fluid phase for slightly depolymerized melts ($\frac{nbo}{t}$ = 0.05 to 0.15). Our data allow quantitative predictions of the sulfur yield of explosive volcanic eruptions over a wide range of magma compositions.

1. Introduction

Sulfur compounds (H_2S and SO_2) constitute a major fraction of volcanic gas emissions, with abundance next only to H_2O and CO_2 (Symonds et al., 1994). The average annual sulfur degassing from volcanoes may add up to 35 % of the total atmospheric SO_2 and sulfate burden, including anthropogenic and ocean sources (Graf et al., 1997). Explosive eruptions can inject large amounts of sulfur into the stratosphere in a single event, inducing atmospheric perturbations that may eventually result in changes of the Earth's average temperature. Once injected into the stratosphere, SO_2 is photochemically oxidized to sulfate aerosols that increase the Earth's albedo by backscattering the incoming solar radiation, while at the same time, they warm the stratosphere by absorbing the upwelling infrared radiation (McCormick et al. 1995). Depending on which of these effects prevails, which in turn depend on the size of the sulfate aerosol particles, the consequences can be either the cooling or warming of the Earth's surface (Lacis et al., 1992). The 1991 eruption of Mt. Pinatubo produced one of the largest climate perturbations of the 20th century, by injecting around 17-20 Tg of SO_2 into the stratosphere that were responsible for a global cooling of 0.5 ˚C (McCormick et al., 1995; Robock, 2002). The amount of sulfur

erupted by Mt. Pinatubo has been estimated to be ~23 larger than the amount that could have been dissolved in the volume of erupted melt at the pre-eruptive T, P, and fO_2 (Gerlach et al., 1996). As for Mt. Pinatubo, many other recent eruptions emitted larger amounts of sulfur than the amount expected from the degassing of the erupted silicate melt (Wallace, 2001 and references therein). The mismatch between the amount of sulfur predicted for an eruption (based on a petrologic estimate of the sulfur content in the erupted melt) and the actual mass discharged is usually called the "sulfur excess" (Andres, 1991) and it has been explained by the accumulation of a sulfur-rich fluid phase in the magma chamber before the eruptions (Keppler, 1999).

In addition to the fluid phase, sulfur can be stored in a magma either as a dissolved species in the silicate melt or in accessory minerals, such as pyrrhotite ($Fe_{(1-x)}S$) and anhydrite ($CaSO_4$). The sulfur contained in these minerals is likely not released into the fluid during explosive eruptions, because their decomposition rate is slow relative to the eruptive timescale (Hanic et al., 1985). However, the solubility of minerals such as anhydrite controls the concentration of sulfur in the melt and, indirectly, the amount of sulfur that partitions in the fluid. An accurate determination of the fluid-melt partition coefficient of sulfur is essential to determine the sulfur distribution among the magmatic phases (melt, fluid and minerals) and, ultimately, the sulfur budget of volcanic eruptions.

There is a broad consensus among available experimental studies on the striking effect of oxygen fugacity on the fluid-melt partition coefficient, which decreases by about an order of magnitude with increasing fO_2 (e.g. Keppler 1999; Webster and Botcharnikov, 2011 and references therein; Zajacz et al. 2012; Jego and Dasgupta, 2014). Sulfur partition coefficients for most of arc magmas at oxidizing conditions are however limited to a few compositions and large uncertainties sometimes exist because of various experimental difficulties. Some recent experimental studies provided insightful data for the partitioning of sulfur between fluid and melt in basaltic (Lesne et al., 2011), andesitic (Zajacz et al., 2012; Fiege et al., 2014), haplogranitic (Keppler, 2010; Huang and Keppler, 2015) and other simplified aluminosilicate melts (Zajacz, 2015). These studies investigated the behavior of sulfur either alone, or in presence of other volatiles, at either isobaric conditions or during decompression, and altogether they suggest that the composition of the silicate melt has a key role on sulfur partitioning between fluid and melt. The full range of melt composition and temperature relevant to differentiated arc magmas remains yet

uncovered. Since these magmas are the main source of volcanogenic sulfur in the stratosphere (e.g., Oppenheimer et al. 2011), reliable data on fluid-melt sulfur partitioning are required in order to predict the environmental impact of explosive eruptions.

In this study, we experimentally determined the fluid-melt partition coefficients of sulfur in differentiated arc magma compositions at oxidizing conditions and for a range of relevant temperatures. By combining our data with experimental data from the literature fulfilling certain criteria (i.e., fluid/melt ratio ~1, multiple experiments with same melt composition that obey Henry's law), we calibrated a general model to predict the sulfur partitioning between fluid and melt. This model, taken together with the anhydrite solubility model presented in Masotta and Keppler (2015), allows calculating the budget of sulfur for most of differentiated arc magmas and, ultimately, the atmospheric sulfur yield of volcanic eruptions.

2. Experimental methods

2.1 High pressure experiments

Seven glassy starting materials were synthetized using as target the composition of the interstitial melt of anhydrite solubility experiments selected from those reported in Masotta and Keppler (2015). Each glass was prepared from a stoichiometric mixture (about 10 g) of analytical grade SiO_2, TiO_2, $Al(OH)_3$, Fe_2O_3, $Mg(OH)_2$, $CaCO_3$, Na_2CO_3, and K_2CO_3. Each mixture was first dehydrated and decarbonated by slowly heating to 1100 ˚C in 12 hours and holding at the same temperature for a further 12 hours, then melted for 2 hours at 1600˚C in a iron-saturated platinum crucible, and finally quenched in distilled water. The resulting glasses were free of crystals and very similar in composition to the experimental glasses selected as target (Table 1).

Each glass was crushed into powder and loaded into 20 mm long gold capsules (2.5 mm outer diameter, 2.1 mm inner diameter) with an equal amount (~10 mg) of H_2SO_4 solution at concentration ranging from 0.05 to 4M (a total of 8 capsules for each starting composition; Table 2). Capsules were then sealed by arc welding and checked for weight loss after heating in a drying furnace for few hours at 130˚C. The high fluid/melt ratio (1:1 by weight) was chosen in order to allow a more accurate determination of the amount of sulfur in the fluid (calculated by mass balance) and,

by consequence, to reduce the error in determining the fluid/melt partition coefficients (see Zajacz et al., 2012). In each experiment, two capsules were loaded into a 30 mm long outer capsule (5 mm outer diameter, 4.6 mm inner diameter) together with 40 mg of water and 400 mg of Re-ReO_2 buffer (1:1 mixture). The high permeability of gold to hydrogen at high temperatures allows the equilibration with the external buffer within few hours or days (Chou, 1986; Keppler, 2010). At the same time, the use of gold capsules precludes significant loss of sulfur through the capsule (Keppler, 2010). Capsules were heated again in a drying furnace at 130˚C for few hours before and after the experiments, and weight-checked for leaks. None of the capsules showed significant weight loss.

Experiments were performed in rapid-quench TZM (Ti and Zr reinforced molybdenum) vessels using argon as pressure medium. The outer capsule was placed on top of a filler rod that was held in the hot zone of the autoclave by an external magnet during the experiment and was dropped for quenching. Pressure was measured with a mechanical gauge with a precision of ±50 bars. Temperature was measured with an external type K thermocouple in the furnace, calibrated against an internal thermocouple. Temperatures within the hot zone are accurate to ±20˚C or better. At the end of each experiment the buffer capsule was pierced and weighed to check the presence of water and the buffer was analyzed by X-ray diffraction to check that both phases were present. Experiments that showed weight loss or failed to quench were discarded.

All the experiments (Table 1) were equilibrated for one week at the same temperature and pressure conditions as the corresponding experiment in Masotta and Keppler (2015). Ideally, this procedure should result in run products containing only glass (quenched melt) and fluid. The absence or low abundance of crystalline phases is an important prerequisite for determining sulfur partition coefficients with high precision. Only few experimental samples showed an unexpectedly high crystal content, due to the high sulfur concentration in the fluid. These experiments were not used for the calculation of partition coefficients (see results section).

2.2 Analytical techniques

Quenched samples were mounted in epoxy and polished for analysis with the electron microprobe. Chemical analyses on crystals and glasses were performed using a JEOL JXA-8200 microprobe, using a 5-10 µm defocused beam, an accelerating voltage of

15 kV and a current of 15 nA. Sulfur was analyzed using a 10 µm defocused beam, an accelerating voltage of 20 kV and a current of 50 nA. Standards used include albite (Si, Na), rutile (Ti), spinel (Al), andradite (Ca, Fe), forsterite (Mg), orthoclase (K) and barium sulfate (S). Alkalis were analyzed before other elements to minimize loss during analysis.

Raman spectra were collected on fluid and gas phases of the synthetic fluid inclusions using a Horiba Jobin Yvon LabRAM HR800 spectrometer with a Peltier-cooled CCD detector. The acquisition setup involved a 514.54 nm Ar laser of 200 mV output power, a confocal pinhole of 500 µm diameter, a 50x magnification objective lens and 1800 mm^{-1} grating.

2.3 Composition of the fluid phase

The mass of sulfur in the fluid phase (S^{fluid}) was calculated by mass balance, by subtracting the amount of sulfur sequestered by anhydrite ($S^{anhydrite}$) and the sulfur dissolved in the melt (S^{melt}) from the bulk sulfur in the H_2SO_4 solution (S^{bulk}) added to the capsule [$S^{fluid} = S^{bulk} - S^{anhydrite} - S^{melt}$]. Some water also dissolves from the fluid into the melt, but this effect is compensated by the dissolution of silicates in the fluid phase (Keppler, 2010). For this reason, no correction for the dissolution of water in the melt phase was applied to the mass of the fluid. The uncertainty of this calculation results mostly from the determination of the amount of anhydrite and of the melt fraction in the samples. The amount of anhydrite in each experiment was calculated by mass balance using the CaO concentration in the melt as the only constraint and assuming that anhydrite is the only CaO-bearing mineral present (the contribution from other Ca-bearing minerals is negligible). These estimates were verified by image analyses of some run products obtained using the free WEB software package ImageJ (Image Processing and Analysis in Java; http://rsb.info.nih.gov/ij/), which in many cases indicated amounts of anhydrite comparable or lower than those determined by mass balance (Table 2). The image analysis often underestimates the amount of anhydrite, because of the uneven distribution in the melt (e.g., some anhydrite may have crystallized at the edge of the capsule and was in part lost during sample preparation). For this reason, the mass balance calculation based on melt composition was preferred over the image analysis to determine of the amount of anhydrite. Image analysis was, however, used to determine the melt fraction in each sample, required to calculate the S^{melt}.

As shown in Table 2, at low anhydrite content (<2 wt.%), the concentration of sulfur in the fluid determined by mass balance is similar to or only slightly lower than the bulk sulfur content of the solution In this case, the amount of sulfur subtracted from the S^{bulk} is generally less than 10 %, thus making the determination of the partition coefficient very robust. With increasing abundance of anhydrite, particularly for samples with high bulk sulfur concentration (e.g., sample A18), the mass-balance correction to the sulfur content of the fluid becomes more significant. For this reason, the few experiments that showed excessively high anhydrite abundance (>6 wt.%) or where the estimates of S^{fluid} appeared unreliable were not used to calculate fluid-melt partition coefficients.

An independent quantification of the sulfur concentration in the fluid was obtained using the Raman-based calibration of Binder and Keppler (2011). The calibration is based on the ratio of the integral areas (I_x) of the main absorption bands of sulfur species (H_2S, SO_2, HSO_4^-, SO_4^{2-}) over the integral area (I_{H2O}) of the water band at 1640 cm^{-1}. The determination of sulfur content in the fluid using this technique is generally consistent with the mass balance estimates at relatively low concentration of sulfur (i.e., S below 1.5 wt.%), though being slightly lower due to the presence of some sulfur species others than those calibrated in Binder and Keppler (2011). At sulfur concentration higher than 1.5 wt.% the bulk sulfur content is systematically underestimated, because of the precipitation of anhydrite and elemental sulfur in the fluid (Table 2). Due to the fact that elemental sulfur and anhydrite may have formed after quench, only Raman estimates at low sulfur concentration can be considered reliable. These estimates at low sulfur content are consistent with the mass balance determination of the S^{fluid}, but still they have a larger uncertainty. Even if Raman analyses cannot be used to determine the S^{fluid} in all the experiments, they provide a further check to the reliability of the mass balance and also valuable insights in sulfur speciation in the quenched fluid.

3. Results

3.1 Texture and composition of phases

All the run products contained a quenched fluid phase, glass and often minerals in abundance of less than 10 vol.% (Figure 1). Fluid inclusions were homogeneously

237 distributed in the samples. As mentioned above, the experimental conditions for each
238 starting composition were the same as for the original phase equilibria experiments
239 reported in Masotta and Keppler (2015), from which interstitial glasses were selected
240 as target composition (Table 1). Theoretically, this should have produced experiments
241 with only glass, however anhydrite was often observed in the run products, as well as
242 minor amounts of oxides, clinopyroxene, amphibole and feldspar. The presence of
243 anhydrite and minor amounts of other minerals is due to the fact that these
244 experiments used a much higher fluid/melt ratio than the original runs, so that
245 partitioning of some components into the fluid may have slightly shifted the stability
246 of crystalline phases. Moreover, the total sulfur concentration in the fluid is often
247 much higher than in the target experiment. This stabilized anhydrite in variable
248 amounts. As result, some of the experimental glasses are more differentiated than the
249 composition of the starting material and the overall compositional range includes the
250 trachyte and rhyolite field of the TAS diagram (Table 3; Figure 2a).
251 Anhydrite crystallized in many of the experiments, usually at concentration of the
252 H_2SO_4 solution higher than 0.4M (Figure 1a). In the experiments performed with the
253 more Ca-rich starting compositions (A18 and D11), anhydrite abundance increases up
254 to 11 wt.% when the solution used is 4M. Mainly as result of anhydrite crystallization,
255 some of these experiments show a much wider compositional variation than expected.
256 The decrease of CaO concentration in the melt with increasing anhydrite abundance
257 produces an increase of SO_3 (Huang and Keppler, 2015). As result of the
258 compositional variation, the solubility product of anhydrite also changes, though
259 being always consistent with the solubility product predicted by the model of Masotta
260 and Keppler (2015) (Figure 2b). The accurate prediction of the anhydrite solubility
261 product for all the anhydrite-saturated experiments demonstrates the attainment of
262 equilibrium during the experiment.
263 Fluid inclusions consisting of a liquid and a gas phase were observed in almost all of
264 the samples. Native sulfur and (in minor amount) anhydrite precipitated at higher
265 sulfur concentration in the fluid (>1.5% wt.%; Figure 1b).
266
267 *3.2 Sulfur species in the quenched fluid*
268 Raman spectra revealed that the sulfur in the quenched fluid is mostly oxidized to S^{6+}
269 (Figure 3). The dominant sulfate species in the fluid are SO_4^{2-} and HSO_4^-, as indicated
270 by their stretching vibrations at 980 cm^{-1} and 1050 cm^{-1}. Some fluid inclusions

contain reduced sulfur in the form of H_2S and HS^-, as shown by the stretching bands at 2570-2590 cm^{-1} (Frezzotti et al., 2012). Only few fluid inclusions contain minor amounts of SO_2, which has a stretching vibration at 1151 cm^{-1} (Binder and Keppler, 2011). A sharp band at ca. 1004-1006 cm^{-1} is observed in most of the samples and likely due to the S-O symmetric stretching vibration of the thiosulfate ion $S_2O_3^{2-}$ (El-Hinnawi et al., 1985). The intensity of the $S_2O_3^{2-}$ peak is generally higher in samples with higher concentration of Na_2O and K_2O in the melt (A13 and A15). In these samples, the stretching band of HSO_4^- at 1050 cm^{-1} is always absent and sulfur occurs as SO_4^{2-} and H_2S-HS^- (Figure 3a). Conversely, sulfur contained in fluid inclusions from all the other experiments with dacitic to rhyolitic composition (series D5, D11 and RD12) is present as HSO_4^- and SO_4^{2-} (Figure 3b-c).

Some spectra showed a band at 1017 cm^{-1}, due to presence of small anhydrite crystals moving within the fluid during laser irradiation. Additional spectra were also collected on crystals sometimes observed inside the gas bubble in inclusions. Sharp bands at ca. 220 and 474 cm^{-1} show that this phase is orthorhombic sulfur (Pasteris et al. 2001; Giuliani et al. 2003; Figure 3d). The presence of anhydrite and elemental sulfur in the fluid inclusion, as well as of thiosulfate, may account for the deviation of the Raman estimates from the mass balance calculation of the total amount of sulfur, at sulfur content higher than 1.5% (Figure 4), since these species could not be quantified.

3.3 Fluid-melt partition coefficients

The fluid-melt partition coefficient of sulfur ($D_S^{fluid/melt}$) is calculated as the ratio between the sulfur concentration in the fluid phase, as determined by mass balance, and the sulfur concentration in the melt. As discussed above, some experiments with higher initial sulfur concentration showed a very large amount of anhydrite and/or a final melt composition very different from the starting glass. For these experiments, it was not possible to determine with a reasonable accuracy the sulfur concentration in the fluid and they were not used to determine the $D_S^{fluid/melt}$ (Table 2). The $D_S^{fluid/melt}$ was calculated for each set of experiments using a weighted least square regression method. Figures 5, 6 and 7 show plots of the sulfur concentration in the melt versus the sulfur concentration in the fluid for runs carried out with different bulk sulfur content under otherwise identical conditions. All the data appear to obey Henry´s law.

Note that data for runs without (open symbols) and with anhydrite (grey symbols) fall on the same line, confirming the reliability of the mass balance calculation of S^{fluid}. The trachytic starting compositions show lower $D_S^{fluid/melt}$ compared to the other more differentiated compositions. Experiments performed at 950˚C (A18) yield a $D_S^{fluid/melt}$ of 1.5±0.3, whereas those performed with the more differentiated melts at 900˚C (A13) and 850˚C (A15) show $D_S^{fluid/melt}$ of 17±3 and 20±8, respectively (Figure 5). Experiments with the dacitic starting compositions (D5 and D11) yield $D_S^{fluid/melt}$ of 20±11 at 900˚C and 95±24 at 850˚C (Figure 6), whereas those with the rhyodacitic compositions (RD11 and RD12) yield $D_S^{fluid/melt}$ of 101±19 at 900˚C and 114±43 at 800˚C (Figure 7).

4. Discussion

4.1 Sulfur speciation in the fluid at low temperature

Raman spectra collected on the fluid inclusions revealed that most of the sulfur in the fluid of the more alkali-rich trachytic samples is present as SO_4^{2-} and H_2S, whereas in dacitic and rhyolitic samples, sulfur occurs mostly as HSO_4^- and SO_4^{2-} (Figure 3). The relative abundance of these species was determined using the calibration by Binder and Keppler (2011). This showed that the absolute abundance of SO_4^{2-} is generally much smaller than that of HSO_4^- and H_2S, and also that the abundance of one of these two species increases with the overall increasing abundance of sulfur (Figure 8). For example, the ratio HSO_4^-/SO_4^{2-} in dacitic-rhyolitic samples increases from 1 to about 20, at increasing bulk sulfur concentration (up to 2 wt.%).

The proportion among the different sulfur species measured at room temperature do not represent sulfur speciation at the experimental temperature, because of the re-equilibration of the aqueous solution at room temperature and the late formation of thiosulfate ($S_2O_3^{2-}$) and elemental sulfur (S_8). The coexistence between S^{6+} species (SO_4^{2-} and HSO_4^-) with S^{2-} (H_2S) is also unlikely to reflect the high-temperature equilibrium. More likely, SO_2 was abundant at high temperature and disproportionated during cooling into H_2S and HSO_4^- (e.g. Rye, 2005)

$$4\ SO_2 + 4\ H_2O = H_2S + 3\ HSO_4^- + 3\ H^+$$

Similar reactions may also be responsible for the formation of elemental sulfur (e.g. Kusakabe et al., 2000). Since all the systems studied here contain iron, redox exchange reactions between iron and sulfur during quenching are also possible; the presence of iron may also have catalyzed the formation of thiosulfate, which was not observed in the iron-free system studied by Binder and Keppler (2011). The fluid speciation observed here may, however, provide information on the relation between melt composition and oxidation state of the fluids at temperature typical of volcanic hydrothermal systems (e.g., Capasso et al., 2014).

Thiosulfates are common constituents of hydrothermal waters in volcanic environment (Webster, 1987; Xu et al., 1998), but they are never observed during in-situ experiments because of their instability above 200˚C (Pokrovski and Dubrovinski, 2011; Ni and Keppler, 2012; Jacquemet et al., 2014). Similarly, solid elemental sulfur (S_8) is stable only at temperature below 100˚C and forms a separate phase in the more sulfur-rich fluid inclusions due to its very low solubility (Boulegue, 1978). Therefore, it is unlikely that either thiosulfate or elemental sulfur were abundant species at the experimental temperatures, where hydrated sulfate species and SO_2 likely dominated (Ni and Keppler, 2012). The formation of thiosulfate during cooling of the fluid may however have contributed to changing the speciation of sulfur in the fluid. Here, it is worth noting that the intensity of the thiosulfate band is generally higher in the trachytic samples, where the average oxidation state of sulfur appears to be lower (Figure 8). In industry, the most frequently used path of synthesis of thiosulfate is the reaction of H_2S or HS^- with HSO_3^- ions (e.g. Greenwood and Earnshaw, 1984):

$$2\ HS^- + 4\ HSO_3^- = 3\ S_2O_3^{2-} + 3\ H_2O$$

HSO_3^- ions may form by reaction of SO_2 with alkali-bearing solutions; the high alkali content of the trachytic melts may therefore have enhanced this reaction. At low temperature, thiosulfate ions may also form by the disproportionation of elemental sulfur in alkaline solutions according to the reaction (Pryor, 1962; Giggenbach, 1974):

$$4S + 3H_2O = S_2O_3^{2-} + HS^- + 4H^+$$

4.2 Compositional dependence of $D_S^{fluid/melt}$ and model calibration

The $D_S^{fluid/melt}$ increases exponentially with the increasing degree of differentiation of the melt, also expressed by the decrease of the non-bridging oxygen per tetrahedron ($\frac{nbo}{t}$, a structural parameter that indicates the degree of melt polymerization; Figure 9a). This observation is consistent with recent experiments by Zajacz (2015) and also with data from Webster et al. (2009), who found a similar correlation of the partition coefficient with the Larson Index of differentiation. In addition to melt polymerization, the Alumina Saturation Index (ASI, a compositional parameter that discriminates between peraluminous and peralkaline melts) shows a positive correlation with the $D_S^{fluid/melt}$ (Figure 9b). This observation is in agreement with experimental observations by Binder (2007), Zajacz et al. (2013) and Huang and Keppler (2014), showing that the ASI controls most of the variation of the $D_S^{fluid/melt}$ in highly polymerized melts (i.e., at very low $\frac{nbo}{t}$). Compared to $\frac{nbo}{t}$ and ASI, temperature has a rather small effect that could be indirectly related to the change in melt composition. The effect of pressure and water concentration in the melt on sulfur partitioning is not considered, because all the experiments are performed at same pressure (200 MPa) and water-saturated conditions. Experimental results in Keppler (2010) suggest that in the range of 50-300 MPa, pressure has a negligible effect on the $D_S^{fluid/melt}$. Implicitly, these experiments suggest that the effect of water content is also subordinate, as long as the system is water-saturated.

A number of previous studies have reported fluid-melt partition coefficients of sulfur under oxidizing conditions (i.e., fO_2 one log unit above Ni-NiO or higher, where S^{6+} is stable in the melt) for andesitic to rhyolitic magmas (Webster and Botcharnikov, 2011 and references therein). However, the quality of the data from different studies is quite variable. We have (i) done experiments with high fluid/melt ratio to reduce errors in the mass balance calculation of the S^{fluid} and (ii) derived $D_S^{fluid/melt}$ from a regression of data points measured with different bulk sulfur content to obtain a higher precision than can be obtained by just measuring a single data point. Moreover, we have (iii) used Raman spectroscopy to validate (where possible) the composition of the fluid determined by mass balance. There are no data in the literature that would fulfill all three of these conditions. The data that probably come closest to our approach are those of Keppler (2010) and Huang and Keppler (2015) for haplogranitic compositions, and of Zajacz et al. (2012) for andesitic compositions. We therefore

included these experimental data in the calibration of a general model for predicting the fluid-melt partitioning of sulfur under oxidizing conditions. The best fit of the available data was obtained by the following equation:

$$\ln\left(D_S^{fluid/melt}\right) = 9.2 - 31.4 \cdot \frac{nbo}{t} - 1.8 \cdot ASI - 29.5 \cdot Al\# + 4.2 \cdot Ca\#$$

where the parameter $\frac{nbo}{t}$ is calculated following Mysen and Richet (2005) (see Masotta and Keppler, 2015 for further details on calculation), ASI is calculated by the molar ratio $\frac{X_{Al2O3}}{X_{CaO}+X_{Na2O}+X_{K2O}}$, Al# and Ca# are two additional compositional parameters calculated using the molar fraction of oxides in the melt $Al\# = \frac{X_{Al2O3}}{X_{SiO2}+X_{TiO2}+X_{Al2O3}}$ and $Ca\# = \frac{X_{CaO}}{X_{Na2O}+X_{K2O}}$, respectively.

The calibration of the $\ln(D_S^{fluid/melt})$ yields an error of estimate (SE) of 0.29 (Figure 10a). The inclusion of the parameter Al# and Ca# was inspired by the observation of Zajacz (2015) that the partitioning behavior of sulfur is very different for alumino-silicate melts containing CaO and Na_2O. Temperature is not included as a parameter in the model despite the fact that the experiments used for its calibration cover a temperature range from 800 to 950 ˚C. Indeed, inclusion of a temperature term in the regression, either isolated or as product with one of the compositional parameters does not improve the fit. This suggests that the intrinsic temperature dependence of sulfur partitioning is negligible, in agreement with observations by Keppler (2010). While all parameters included in the model refer to the melt composition, this does not imply that the fluid has no effect on the partitioning; rather, the fluid properties are buffered and controlled by the composition of the melt. Indeed, the Raman data suggest that, at least at low temperature, there are major changes in sulfur speciation in fluids coexisting with melts of different composition (Figure 8).

The above model should allow a reliable prediction of the fluid melt partitioning of sulfur for andesitic to rhyolitic melts at an oxygen fugacity one log unit above Ni-NiO and higher, at temperatures up to 1100 ˚C and at pressures up to 300 MPa. It should not be used outside the range where it is calibrated, e.g. not for pressures below 100 MPa and not for strongly peralkaline melts. Within the range of calibration, the model predicts with a reasonably good accuracy (SE=0.78) the partition coefficient of a test

436 dataset (Fiege et al., 2014; Binder, 2011; Webster et al., 2011; Figure 10b).
437 Experiments from Webster et al. (2009) on trachytic to phonolitic melts were also
438 used as test for the model, but not shown in Figure 10b; the prediction for these data
439 was still broadly consistent with the measurements, but much less accurate, possibly
440 due to the fact that the experiments used a lower fluid/melt ratio and highly
441 concentrated saline fluids.
442
443 *4.3 Sulfur distribution among anhydrite, melt and fluid*
444 The anhydrite solubility product measured in the run product glasses is always in
445 agreement with the prediction of the anhydrite solubility model by Masotta and
446 Keppler (2015), confirming that equilibrium conditions were achieved in all the
447 experiments (Figure 2). Sulfur concentration and anhydrite abundance are both
448 significantly higher in the less polymerized melts. For example, in the trachy-andesite
449 (sample A18), the SO_3 concentration in the melt reaches 0.70 wt.% and anhydrite
450 abundance can be up to 11 wt.%, whereas in the rhyolite (sample RD11) the SO_3
451 concentration can be as low as 0.01 wt.% and anhydrite is always less than 1.5%
452 (Table 2). The high abundance of anhydrite in the trachytic melt is somehow
453 unexpected, given the much higher solubility of anhydrite in this melt compared to the
454 rhyolite (Figure 2). This is, however, consistent with the surprisingly low fluid-melt
455 partition coefficient determined for the trachyte, where up to three quarters of the bulk
456 sulfur is sequestered by anhydrite and only a small fraction remains in fluid and melt.
457 It should be also noted that, even without subtracting the amount of sulfur contained
458 in anhydrite from the bulk sulfur in the capsule, the partition coefficients of the
459 experiments reported in Figure 5 would still remain very low (<25), because of the
460 high concentration of sulfur in the melt. The effect of this subtraction is much smaller
461 in the more polymerized rhyolitic melts, where anhydrite is generally scarce and most
462 of the sulfur partitions into the fluid (the sulfur concentration in the fluid calculated
463 using the mass balance is very similar to the total sulfur in the capsule; Table 2).
464 Because of the apparent increase of anhydrite abundance in less polymerized melts,
465 our experiments may at first sight give a misleading impression of the actual balance
466 of sulfur in differentiated arc magma. The formation of abundant anhydrite in our
467 experiments is due to the relatively high bulk sulfur content (SO_3 ~1-10 wt.%) and the
468 high fluid/melt ratio (~1), which is uncommon in real magmas. At experimental
469 conditions, most of the sulfur is contained either in anhydrite or in the fluid (Figure

11a). At conditions more realistic for oxidized, differentiated arc magmas (e.g., bulk SO_3 of 0.1-1 wt.%, fluid/melt ratio of 0.01-0.1), melt polymerization controls the distribution of sulfur, either into melt and anhydrite (for depolymerized melts) or into anhydrite and fluid (for polymerized melts) (Figure 11b). The overall implication of the sulfur distribution observed is therefore consistent with the conclusion by Masotta and Keppler (2015) that sulfur sequestration by anhydrite is less efficient in depolymerized melts. In these melts, because of the low partition coefficient, the balance of sulfur is mostly controlled by the solubility of anhydrite. Conversely, the high fluid-melt partition coefficient and low anhydrite solubility for polymerized melts implies that the sulfur balance in these melts is much more affected by the fraction of fluid in the system, with the sulfur sequestration by anhydrite being more efficient at lower fluid fractions.

4.4 Sulfur budget in differentiated arc magmas

The overall variation of the partition coefficients in the investigated melt composition is quite large (2 to 120) and occurs in a relatively small range of melt compositions ($\frac{nbo}{t}$ ranging from 0 to 0.15). In particular, the largest increase is observed at the transition between the dacite and rhyodacite (sample D11 and D5), with the partition coefficient increasing from 20 to about 100 (Figure 6). This indicates that the distribution of sulfur may change significantly even with rather subtle variations of magma composition during crystallization.

In order to see the effect of melt differentiation and quantify the budget of sulfur in magmas, the variation of both $D_S^{fluid/melt}$ and anhydrite solubility with melt composition must be considered. Hence, combining the model of partition coefficients presented in this work with the anhydrite solubility model of Masotta and Keppler (2015), we have calculated this budget for some of the arc magmas feeding sulfur-rich eruptions, such as the 1982 El Chichòn trachy-andesite, the Huerto Andesite (Fish Canyon System, San Juan Volcanic Field), the 1980 St. Helens dacite, and the 1991 Mt. Pinatubo dacite (Figure 12). The budget is calculated over the range of differentiation of these magmas, as determined from phase equilibria experiments available in the literature (El Chichòn and St. Helens, Carroll and Rutherford, 1987; Mt. Pinatubo, Scaillet and Evans, 1999; Huerto Andesite, Parat et al., 2008). In all the magmas considered, the increase of melt polymerization upon differentiation reduces

503 the solubility of anhydrite and increases the partitioning of sulfur in the fluid. The
504 contrasting effects of melt polymerization on anhydrite solubility and fluid-melt
505 partitioning is clearly shown by the change in slope of the curves for the fraction of
506 sulfur in the melt (X_S^{melt}) and the fraction of sulfur in anhydrite ($X_S^{anhydrite}$) at $\frac{nbo}{t}$
507 between 0.05 and 0.15 (Figure 12). The tradeoff between anhydrite solubility and
508 fluid-melt partitioning determines in this range a maximum of the sulfur fraction in
509 the fluid (X_S^{fluid}). The position of this maximum varies slightly as a function of melt
510 composition and total sulfur concentration, whereas its height is proportional to the
511 fluid fraction in the system. In the examples reported in Figure 12, the sulfur fraction
512 in the fluid has always a maximum at $\frac{nbo}{t}$ between 0.05 and 0.10, which is generally
513 close to the $\frac{nbo}{t}$ of the magma at the eruptive conditions determined from phase
514 equilibria experiments (yellow stars in Figure 12). The only exception is the eruption
515 of El Chichòn, for which the pre-eruptive conditions indicate an efficient sulfur
516 sequestration by anhydrite (crystallization of ~ 2 wt.% anhydrite) and a rather small
517 fraction of the total sulfur being in the fluid. As we show in the next section, the large
518 sulfur yield of El Chichòn eruption may be due to the rather high bulk sulfur
519 concentration in the system and to the eruption of a separate fluid phase that had
520 extracted sulfur from a large volume of magma.
521 The evolution of the sulfur distribution modeled in Figure 12 assumes that magma
522 differentiation occurs in a closed system, with the bulk sulfur content being constant
523 over time. If open system degassing is allowed, the constant fractionation of the fluid
524 phase would cause a progressive loss of sulfur, as due to the preferential partitioning
525 of sulfur in the fluid with magma differentiation. At such conditions, anhydrite may
526 no longer be stable and larger continuous sulfur emissions are expected from yet
527 undifferentiated magmas ($\frac{nbo}{t} > 0.15$) if the sulfur is efficiently transferred from the
528 melt to the fluid.
529
530 *4.5 Implications for sulfur release and excess during eruptions*
531 The amount of sulfur released during explosive eruptions is often larger than the
532 amount of sulfur initially contained in the erupted melt. This paradox has been
533 referred to as the sulfur excess and it has been explained by the presence of a fluid

phase that is erupted together with the magma (Keppler, 1999; Wallace, 2001). The sulfur excess can be calculated according to Keppler (2010):

$$E = \frac{f D_S^{fluid/melt}}{x}$$

where f represents the fraction of fluid in the magma and x is the fraction of erupted melt relative to the total amount of melt in the magma chamber. According to this equation, at a given fluid and melt fractions, the sulfur excess depends only on the sulfur partition coefficient or, indirectly, on the degree of melt polymerization.

Similarly to what shown for the sulfur budget, we have modeled the partition coefficient and the sulfur excess for the 1980 eruption of St. Helens, the 1982 eruption of El Chichòn and the 1991 eruption of Mt. Pinatubo, assuming a fraction of erupted melt x = 0.20 (value expected for a 5 km deep reservoir; Acocella and Scandone, 2007) and pre-eruptive conditions as determined from phase equilibria experiments (Figure 13). The sulfur excess associated to these eruptions is ~20-25 for St. Helens and Mt. Pinatubo (Gerlach and McGee, 1994; Gerlach et al., 1996) and ~70 for El Chichòn (Devine et al., 1984). The dacite of Mt. Pinatubo at 780˚C (Scaillet and Evans, 1999) shows the highest partition coefficient ($D_S^{fluid/melt}$ ~ 200) and a relatively small fluid fraction (f = 0.02) is sufficient to explain the sulfur excess. The dacite of St. Helens at 900˚C (Rutherford, 1993) yields a lower partition coefficient ($D_S^{fluid/melt}$ ~ 60) and suggests that a slightly larger fluid fraction (f = 0.08) was present in the magma before the eruption. The trachy-andesite of El Chichòn at 800˚C (Carroll and Rutherford, 1987) yields a high partition coefficient ($D_S^{fluid/melt}$ ~ 100), nonetheless, a higher fluid fraction (f = 0.14) is required to explain the larger sulfur excess (~70). Such conditions of high fluid fractions are possible if the erupted mass is mostly consisting of bubble-rich magma accumulated in a conduit or during convection (e.g., Shinohara, 2008). Part of the fluids may have separated during the differentiation of the magma and accumulated on the top of the chamber. Interestingly, the trachy-andesite of El Chichòn is the only case in Figure 12 where the pre-eruptive conditions do not fall on the maximum of the X_S^{fluid} curve, but at lower $\frac{nbo}{t}$.

5. Conclusions

The fluid-melt partition coefficient of sulfur was experimentally determined for a range of differentiated arc magma compositions. Trachy-andesitic and dacitic melts show much lower partition coefficients (2-20) than rhyodacitic and rhyolitic melts (80-120). Partition coefficients mostly depend on melt polymerization ($\frac{nbo}{t}$) and other compositional parameters, whereas temperature has a minor effect.

A new model to predict the sulfur partition coefficients was calibrated using structural and compositional parameters of the melt. This model, combined with the anhydrite solubility model of Masotta and Keppler (2015), is used to calculate the sulfur budget for some of the most studied sulfur rich eruptions. At increasing differentiation/melt polymerization, sulfur partition coefficients increase whereas anhydrite solubility decreases. Depending on the total amount of sulfur in the system, sulfur is either preferentially partitioned into the fluid (low concentration) or sequestered by anhydrite (high concentration). Conversely, in less differentiated (depolymerized) melt compositions, most of the sulfur is stored in the melt, because of both the higher solubility of anhydrite and the low sulfur partition coefficients. The interplay between anhydrite solubility and fluid/melt partitioning determines a maximum of the sulfur fraction in the fluid in melts having $\frac{nbo}{t}$ between 0.05 and 0.15.

Acknowledgements

This work was supported by a Humboldt fellowship to MM. We are grateful to Hubert Schulze and Raphael Njul for sample preparation, and to Detlef Krauße for assistance during microprobe analyses. Constructive reviews by Adrian Fiege and by an anonymous referee helped to improve the manuscript.

References

Acocella V. and Scandone R. (2007) Control of the aspect ratio of the chamber roof on caldera formation during silicic eruptions. *Geophys. Res. Lett.* **34**, L22307.

Andres R.J., Rose W.I., Kyle P.R., deSilva S., Francis P., Gardeweg M. and Moreno Roa H. (1991) Excessive sulfur dioxide emissions from Chilean volcanoes. *J. Volcanol. Geotherm. Res.* **46**, 323–329.

597 Binder B. (2007) Experimentelle Untersuchungen zum Verhalten von Schwefel in
598 magmatisch-hydrothermalen Systemen. Ph.D. dissertation, University of
599 Tübingen.
600 Binder B. and Keppler H. (2011) The oxidation state of sulfur in magmatic fluids.
601 *Earth Planet. Sci. Lett.* **301**, 190–198.
602 Boulegue J. (1978) Solubility of elemental sulfur in water at 298K. *Phosporus and*
603 *Sulfur and the Related Elements* **5**, 127–128.
604 Capasso G., Federico C., Madonia P. and Paonita A. (2014) Response of the shallow
605 aquifer of the volcano-hydrothermal system during the recent crises at Vulcano
606 Island (Aeolian Archipelago, Italy). *J. Volcanol. Geotherm. Res.* **273**, 70–80.
607 Chou I.M. (1986) Permeability of precious metals to hydrogen at 2 kbar total pressure
608 and elevated temperatures. *Am. J. Sci.* **286**, 638–658.
609 Devine J.D., Sigurdsson H., Davis A.N. and Self S. (1984) Estimates of sulfur and
610 chlorine yield to the atmosphere from volcanic eruptions and potential climatic
611 effects. *J. Geophys. Res.* **89**, 6309–6325.
612 Devine J.D., Gardner J.E., Brack H.P., Layne G.D. and Rutherford M.J. (1995)
613 Comparison of microanalytical methods for estimating H_2O contents of silicic
614 volcanic glasses. *Am. Mineral.* **80**, 319–328.
615 El-Hinnawi M.A., Peter L. and Meyer B. (1985) Raman spectra of copper(I), silver(I)
616 and gold(I) Cyanides in aqueous solutions of sodium thiosulphate. *J. Raman*
617 *Spectroscopy* **16** (4) 272-279.
618 Fiege A., Behrens H., Holtz F. and Adams F. (2014) Kinetic vs. thermodynamic
619 control of degassing of H_2O-S ± Cl-bearing andesitic melts. *Geochim.*
620 *Cosmochim. Acta* **125**, 241-264.
621 Frezzotti, M.L., Tecce, F., and Casagli, A. (2012) Raman spectroscopy for fluid
622 inclusion analysis. *Journal of Geochemical Exploration* **112**, 1–20.
623 Gerlach T.M. and K.A. McGee (1994) Total sulfur dioxide emissions and pre-
624 eruption vapor-saturated magma at Mount St. Helens, 1980-88. *Geophys. Res.*
625 *Lett.* **21**, 2833-2836.
626 Gerlach T.M., Westrich H.R. and Symonds R.B. (1996) Pre-eruption vapor in magma
627 of the climactic Mount Pinatubo eruption: source of the giant stratospheric sulfur
628 dioxide cloud. Newhall, C.G. & Punongbayan R.S. (eds) *Fire and Mud.*
629 *Eruptions and Lahars of Mount Pinatubo, Philippines*. University of Washington
630 Press, 415-434.

631 Giggenbach W.F. (1974) Equilibria involving polysulfide ions in aqueous sulfide
632 solutions up to 240°C. *Inorganic Chem*. **13**, 1724-1730.
633 Giuliani G., Dubessy J., Banks D., Vinh H.Q., Lhomme T., Pironon J., Garnier V.,
634 Trinh V.T., Long P.V., Ohnenstetter D. and Schwarz, D. (2003) CO_2-H_2S-COS-
635 S_8-AlO(OH)-bearing fluid inclusions in ruby from marble-hosted deposits in Luc
636 Yen area, North Vietnam. *Chemical Geology* **194**, 167–185.
637 Graf H.-F., Feichter J., Langmann B. (1997) Volcanic sulfur emissions: Estimates of
638 source strength and its contribution to the global sulfate distribution. *J*. *Geophys*.
639 *Res*. **102**, 10727-10738.
640 Greenwood N.N. and Earnshaw A. (1984) Chemistry of the Elements. Pergamon
641 Press.
642 Hanic F., Galikova L., Havlica J., Kapralik I. and Ambruz V. (1985) Kinetics of the
643 thermal decomposition of $CaSO_4$ in air. *British Ceramics Transactions and*
644 *Journal* **84**, 22-25.
645 Huang R. and Keppler H. (2014) Anhydrite stability and the effect of Ca on the
646 behavior of sulfur in felsic melts. *Am*. *Mineral*. DOI:
647 http://dx.doi.org/10.2138/am-2015-4959
648 Jacquemet N., Guillaume D., Zwick A. and Pokrovski G.S. (2014) In situ Raman
649 spectroscopy identification of the S_3^- ion in S-rich hydrothermal fluids from
650 synthetic fluid inclusions. *Am*. *Mineral*. **99**, 1109-1118.
651 Jego S. and Dasgupta R. (2014) The fate of sulfur during fluid-present melting of
652 subducting basaltic crust at variable oxygen fugacity. *J*. *Petrol*. **55**, 1019-1050.
653 Keppler H. (1999) Experimental evidence for the source of excess sulfur in explosive
654 volcanic eruptions. *Science* **284**, 1652–1654.
655 Keppler H. (2010) The distribution of sulfur between haplogranitic melts and aqueous
656 fluids. *Geochim*. *Cosmochim*. *Acta* **74**, 645–660.
657 Kusakabe M., Komoda Y., Takano B. and Abiko, T. (2000) Sulfur isotopic effects in
658 the disproportionation reaction of sulfur dioxide in hydrothermal fluids:
659 implications for the $\delta^{34}S$ variations of dissolved bisulfate and elemental sulfur
660 from active crater lakes. *J*. *Volcanol*. *Geothermal Res*. **97**, 287-307.
661 Lacis A., Hansen J.E., Sato M. (1992) Climate forcing by stratospheric aerosols.
662 *Geophys*. *Res*. *Lett*. **19**, 1607–1610.

663 Lesne P., Kohn S.C., Blundy J., Witham F., Botcharnikov R.E. and Behrens H. (2011)
664 Experimental simulation of closed system degassing in the system basalt–H_2O–
665 CO_2–S–Cl. *J*. *Petrol*. **52**, 1737–1762.
666 Masotta M. and Keppler H. Anhydrite solubility in differentiated arc magmas.
667 *Geochim*. *Cosmochim*. *Acta* **158**, 79-102.
668 Mather T.A., Tsanev V.I., Pyle D.M., McGonigle A.J.S., Oppenheimer C., and Allen
669 A.G. (2004) Characterization and evolution of tropospheric plumes from Lascar
670 and Villarrica volcanoes, Chile. *Journal of Geophysical Research* **109**, D21303.
671 Mather T.A., McCabe J.R., Rai V.K., Thiemens M.H., Pyle D.M., Heaton T.H.E.,
672 Sloane H.J. and Fern G.R. (2006) Oxygen and sulfur isotopic composition of
673 volcanic sulfate aerosol at the point of emission. *J*. *Geophys*. *Res*. **111**,
674 doi:10.1029/2005JD006584.
675 McCormick M. P., Thomason L. W. and Trepte C. R. (1995) Atmospheric effects of
676 the Mt Pinatubo eruption. *Nature* **373**, 399–404.
677 Ni. H and Keppler H. (2012) In-situ Raman spectroscopic study of sulfur speciation in
678 oxidized magmatic-hydrothermal fluids. Am. Mineral. **97**, 1348-1353
679 Oppenheimer C., Scaillet B. and Martin R.S. (2011) Sulfur degassing from volcanoes:
680 Source conditions, surveillance, plume chemistry and earth system impacts. *Rev*.
681 *Mineral*. *Geochem*. **73**, 363–421.
682 Parat F., Holtz F. and Feig S. (2008) Pre-eruptive conditions of the Huerto andesite
683 (Fish Canyon System, San Juan Volcanic Field, Colorado): Influence of volatiles
684 (C-O-H-S) on phase equilibria and mineral composition. *J*. *Petrol*. **49**, 911–935.
685 Pasteris J.D., Freeman J.J., Goffredi S.K. and Buck K. (2001) Raman spectroscopic
686 and laser scanning confocal microscopic analysis of sulfur in living sulfur-
687 precipitating marine bacteria. *Chemical Geology* **180**, 3–18.
688 Pokrovski G.S. and Dubrovinsky L.S. (2011) The S_3^- ion is stable in geological fluids
689 at elevated temperatures and pressures. *Science* **331**, 1052–1054.
690 Pryor W.A. (1962) *Mechanisms of Sulfur Reactions*. McGraw-Hill.
691 Robock A. (2002) The climatic aftermath. *Science* **295**, 1242–1244.
692 Rye R.O. (2005) A review of the stable-isotope geochemistry of sulfate minerals in
693 selected igneous environments and related hydrothermal systems. *Chem*. *Geol*.
694 **215**, 5–36.
695 Rutherford M.J. (1993) Experimental petrology applied to volcanic processes. Eos
696 Trans. AGU, 74, 49 and 55.

Scaillet B., Clemente B., Evans B. W. and Pichavant M. (1998) Redox control of sulfur degassing in silicic magmas. *J. Geophys. Res. Solid Earth* **103**, 23937–23949.

Shinohara H. (2008) Excess degassing from volcanoes and its role on eruptive and intrusive activity. *Reviews of Geophysiscs* **46**, RG4005.

Symonds R.B., Rose W.I., Bluth G.J.S. and Gerlach T.M. (1994) Volcanic gas studies: methods, results, and applications. *Rev. Mineral.* **30**, 1–66.

Wallace P.J. (2001) Volcanic SO_2 emissions and the abundance and distribution of exsolved gas in magma bodies. *J. Volcanol. Geothermal Res.* **108**, 85–106.

Webster J.G. (1987) Thiosulfate in surficial geothermal waters, North Island, New Zealand. *Appl. Geochem.* **2**, 579-584.

Webster J.D. (1992) Fluid–melt interactions involving Cl-rich granites: experimental study from 2 to 8 kbar. *Geochim. Cosmochim. Acta* **56**, 659–678.

Webster J.D., Goldoff B. and Shimizu N. (2011) C-O-H-S fluids and granitic magma: how S partitions and modifies CO_2 concentrations of fluid-saturated felsic melt at 200 MPa. *Contrib. Mineral. Petrol.* **162**, 849-865.

Webster J.D., Sintini M.F. and De Vivo B. (2009) The partitioning behavior of Cl, S, and H_2O in aqueous vapor- ± saline-liquid saturated phonolitic and trachytic melts at 200 MPa. *Chem. Geol.* **263**, 19–36.

Webster J.D. and Botcharnikov R.E. (2011) Distribution of sulfur between melt and fluid in S-O-H-C-Cl-bearing magmatic system at shallow crustal pressures and temperatures. *Reviews in Mineralogy and Geology* **263**, 19-36.

Xu Y., Schoonen M.A.A., Nordstrom D.K., Cunningham K.M. and Ball J.W. (1998) Sulfur geochemistry of hydrothermal waters in Yellowstone National Park: I. The origin of thiosulfate in hot spring waters. *Geochim. Cosmochim. Acta* **63**, 3729-3743.

Zajacz Z., Candela P.A., Piccoli P.M. and Sanchez-Valle C. (2012) The partitioning of sulfur and chlorine between andesite melts and magmatic volatiles and the exchange coefficients of major cations. *Geochim. Cosmochim. Acta* **89**, 81-101.

Zajacz Z. (2015) The effect of melt composition on the partitioning of oxidized sulfur between silicate melts and magmatic volatiles. *Geochim. Cosmochim. Acta* **158**, 223-244.

Figure captions

731 Fig.1 – Backscatter electron image of an anhydrite-bearing run product (a) and
732 transmitted light microscope image of a run product with elemental sulfur
733 precipitated in two fluid inclusions (b). The sulfur is the small object inside the
734 gas bubble of the two inclusions.
735 Fig. 2 – Total alkali vs. silica diagram showing the compositional range of the
736 experimental glasses (a). Test of the anhydrite solubility model by Masotta and
737 Keppler (2015) for the anhydrite bearing experiments (b); the good agreement
738 confirms that equilibrium was achieved in all the experiments.
739 Fig. 3 – Selected Raman spectra collected on fluid inclusions from trachyte (sample
740 A15-6) (a), dacite (sample D5-7) (b) and rhyodacite (sample RD12-6) (c)
741 experiments. Intensity is normalized to the ν_1 vibration of H_2O at ~3500 cm^{-1}.
742 Raman spectra of orthorhombic elemental sulfur precipitated from a fluid
743 inclusion (sample D5-6) (d). See text for interpretation of Raman spectra.
744 Fig. 4 – Comparison between sulfur concentration in the fluid determined by mass
745 balance and that determined using Raman spectroscopy. Note that Raman
746 analyses of fluid inclusions in trachyte significantly underestimate the actual
747 amount of sulfur in the fluid; this may be due to higher abundance of thiosulfate,
748 which cannot be quantified by Raman (see text for details).
749 Fig. 5 – Fluid-melt partition coefficients of sulfur determined by weighted least
750 square regression in experiments performed with trachytic samples A18, A13 and
751 A15. Grey symbols refer to anhydrite-saturated experiments.
752 Fig. 6 – Fluid-melt partition coefficients of sulfur determined by weighted least
753 square regression in experiments performed with samples D11 (dacite) and D5
754 (rhyodacite). Grey symbols refer to anhydrite-saturated experiments.
755 Fig. 7 – Fluid-melt partition coefficients of sulfur determined by weighted least
756 square regression in experiments performed with rhyolitic samples RD11 and
757 RD12. Grey symbols refer to anhydrite-saturated experiments.
758 Fig. 8 – Proportion among different sulfur species calculated using the calibration by
759 Binder and Keppler (2011). See text for discussion.
760 Fig. 9 – Dependence of the fluid-melt partition coefficients of sulfur [$\ln(D_S^{fluid/melt})$
761 determined for each of the samples] on melt polymerization (expressed as $\frac{nbo}{t}$) (a)
762 and Alumina Saturation Index (ASI) (b). Note that $\frac{nbo}{t}$ cannot truly be a negative
763 number. When the formula used to calculate $\frac{nbo}{t}$ yields negative numbers, it

indicates that some Al with a coordination number >4 occurs in the silicate melt (Mysen and Richet, 2005).

Fig. 10 – Calibration of the $\ln(D_S^{fluid/melt})$ according to equation presented in the text (a). Test of the model using experiments external to the calibration dataset (experiments from Binder (2011), Webster et al. (2011) and "near-equilibrium" experiments by Fiege et al. (2014) (b).

Fig. 11 – Distribution of sulfur among anhydrite, fluid and melt calculated at the experimental conditions (a) and real magma conditions (b). The comparison of the two diagrams demonstrates the effects of fluid/melt ratio and bulk sulfur content on the distribution of sulfur between different phases.

Fig. 12 – Variation of the sulfur distribution among anhydrite, fluid and melt upon close system differentiation of magmas from different volcanoes (trachy-andesite from El Chichòn, dacite from St. Helens, Huerto Andesite and dacite from Mt. Pinatubo). Sulfur distribution is calculated assuming a fluid fraction of 0.02 and at different $\frac{nbo}{t}$ determined using the melt composition of phase equilibria experiments reported in literature: Carroll and Rutherford (1987) for El Chichòn and St. Helens, Parat et al. (2008) for Huerto Andesite and Scaillet and Evans (1999) for Mt. Pinatubo. Representative bulk sulfur contents (S^{bulk}) are reported for each of the systems. The yellow stars indicate the pre-eruptive conditions inferred for these eruptions. Note that in addition to $\frac{nbo}{t}$, other compositional parameters also change during fractional crystallization and therefore the curves shown do not always follow a simple trend.

Fig. 13 – Variation of the $D_S^{fluid/melt}$ with $\frac{nbo}{t}$ for the magmas of the 1980 eruption of St. Helens, the 1982 eruption of El Chichòn and the 1991 eruption of Mt. Pinatubo (a). Calculation of the sulfur excess according to the equation reported in the text, assuming a melt fraction (x) of 0.20 and different fluid fractions (f). The fluid fractions at pre-eruptive conditions (stars) were chosen as to match the sulfur excess reported in the literature for these eruptions (grey shaded areas) (b).

Table 1. Composition of the starting materials used.

Sample (σ)[1]	**A18**	**(15)**	**A13**	**(15)**	**A15**	**(15)**	**D11**	**(15)**	**D5**	**(15)**	**RD11**	**(15)**	**RD12**	**(15)**
SiO_2	59.16	1.07	63.17	0.79	66.48	1.07	65.99	0.42	69.85	0.93	72.15	1.59	74.38	0.64
TiO_2	0.75	0.05	0.44	0.04	0.62	0.05	0.71	0.04	0.36	0.05	0.55	0.07	0.23	0.07
Al_2O_3	20.27	0.82	20.34	0.46	17.96	0.76	18.82	0.25	17.47	0.49	16.14	1.05	13.80	0.46
FeO	3.13	0.11	1.58	0.14	1.84	0.13	2.28	0.09	1.74	0.13	1.28	0.19	1.22	0.14
MgO	1.38	0.07	0.94	0.08	0.28	0.03	1.50	0.07	0.63	0.04	0.34	0.04	0.28	0.03
CaO	4.78	0.25	2.34	0.16	1.68	0.19	2.50	0.10	1.69	0.14	1.80	0.26	1.06	0.16
Na_2O	6.10	0.10	5.83	0.18	4.70	0.20	5.35	0.08	4.84	0.13	3.57	0.20	3.52	0.10
K_2O	3.63	0.14	4.38	0.16	5.61	0.23	2.08	0.09	2.69	0.06	3.36	0.14	4.62	0.08
Total	99.19		99.03		99.16		99.22		99.27		99.19		99.10	
nbo/t	0.146		0.039		0.030		0.051		0.007		-0.009		0.017	
ASI	0.895		1.094		1.065		1.203		1.253		1.263		1.087	
Experimental conditions of the original phase equilibria experiments (Masotta and Keppler, 2015)														
T (°C)	950		900		850		900		850		900		800	
P (MPa)	195		202		200		200		200		180		200	
H_2O	4.60		4.58		4.35		5.10		4.35		4.09		4.08	
SO_3	2.40		0.99		0.94		1.11		0.94		0.89		0.88	
H_2O^-	8.62		6.81		8.54		6.74		9.63		5.81		6.35	
Liq	0.79		0.59		0.38		0.68		0.55		0.81		0.61	
Pl	0.11		0.25		0.40		0.22		0.34		0.12		0.27	
Cpx	0.08		0.09		0.16		0.00		0.00		0.00		0.00	
Opx	0.00		traces		traces		0.02		traces		0.03		0.08	
Am	0.00		0.03		0.03		0.04		0.08		0.00		0.00	
Ox	0.01		0.02		0.02		0.03		0.02		0.03		0.03	
Anhy	0.01		0.02		0.01		0.01		0.01		0.01		0.01	

[1]σ = standard deviation, the number of analyses is reported in parenthesis

nbo/t = non-bridging oxygen per tetrahedron (calculated following Mysen and Richet, 2005; see text for details)

ASI = Alumina Saturation Index, calculated in molar fraction [$ASI=X_{Al2O3}/(X_{CaO}+X_{Na2O}+X_{K2O})$]

H_2O = amount of water added to the capsule

H_2O^- = amount of water in the melt determined using the "by difference" technique (Devine et al., 1995)

Phase abbreviations: liquid (Liq), plagioclase (Pl), clinopyroxene (Cpx), orthopyroxene (Opx), amphibole (Am), oxide (Ox), anhydrite (Anhy)

Table 2

Table 2. Experimental data on the fluid-melt partitioning of sulfur.

Run	H_2SO_4 (mg)	Sample (mg)	H_2SO_4 (M)	Anhy[1] (wt.%)	Anhy[2] (wt.%)	S^{bulk} (wt.%)	S^{fluid} (wt.%)	S^{fluid}_{Raman} (wt.%)	S^{melt} (wt.%)	σ	$D_S^{fluid/melt}$
A18 - Trachy-andesite (950˚C)					$D^{fluid/melt}$ = 1.5±0.3						
A18-7	10.98	13.08	0.05	-		0.16	0.11		0.049	0.020	2.1
A18-1	9.92	10.38	0.10	-		0.32	0.20		0.122	0.030	1.6
A18-2*	10.39	6.38	0.25	3.39	2.8	0.78	0.26		0.152	0.005	1.7
A18-8*	10.22	10.22	0.40	3.95	3.3	1.23	0.24		0.169	0.003	1.4
A18-3*	10.25	8.54	0.50	6.53	3.5	1.53	0.24		0.179	0.007	1.4
A18-4*	10.87	7.43	1.00	8.47	7.1	2.91	-		0.206	0.004	-
A18-5*	11.38	10.35	2.00	9.94	6.0	5.35	-		0.243	0.009	-
A18-6*	11.69	10.43	4.00	11.02	11.5	9.20	-		0.270	0.006	-
A13 - Trachyte (900˚C)					$D^{fluid/melt}$ = 17±3						
A13-7	11.18	9.93	0.05	-		0.16	0.15		0.008	0.001	19.6
A13-1	9.98	14.12	0.10	-		0.32	0.29		0.023	0.003	12.4
A13-2	10.21	9.77	0.25	-		0.78	0.74		0.048	0.002	15.3
A13-8	10.31	11.10	0.40	-		1.23	1.17		0.066	0.002	17.7
A13-3b*	9.96	11.67	0.50	0.41	0.5	1.53	1.33	0.59	0.088	0.008	15.2
A13-4*	11.86	10.98	1.00	2.02	1.7	2.91	2.44		0.121	0.022	20.1
A13-5*	10.98	10.22	2.00	4.00	3.5	5.35	-		0.153	0.003	-
A13-6*	12.19	10.37	4.00	3.41	2.7	9.20	-		0.174	0.005	-
A15 - Trachyte (850˚C)					$D^{fluid/melt}$ = 21±8						
A15-1	11.62	10.76	0.05	-		0.16	0.15		0.014	0.006	10.2
A15-2	11.67	9.70	0.10	-		0.32	0.28	0.19	0.042	0.001	6.8
A15-3*	10.84	11.67	0.25	0.50	0.7	0.78	0.63		0.043	0.002	14.5
A15-4*	9.65	9.49	0.40	1.00	1.5	1.23	0.98		0.060	0.002	16.2
A15-5*	10.61	10.50	0.50	2.68	2.0	1.53	0.92		0.064	0.003	14.3
A15-6*	10.58	10.38	0.80	2.99	1.7	2.38	1.72	0.54	0.072	0.002	24.0
A15-7*	10.16	10.04	1.00	3.13	3.3	2.92	2.23		0.077	0.005	28.8
A15-8*	10.68	10.74	1.25	5.00	4.8	3.57	2.49		0.091	0.004	27.4
D11 - Dacite (900˚C)					$D^{fluid/melt}$ = 20±11						
D11-7	10.67	12.42	0.05	-		0.16	0.15		0.004	0.001	36.7
D11-1	10.44	11.87	0.10	-		0.32	0.26		0.050	0.004	5.3

D11-2	11.14	11.81	0.25	-		0.78	0.70		0.076	0.011	9.3
D11-8*	10.85	10.69	0.40	0.60	0.7	1.23	1.03	0.70	0.088	0.002	11.6
D11-3	10.40	10.99	0.50	-		1.53	1.45		0.072	0.006	20.1
D11-4*	10.66	9.76	1.00	0.75	0.5	2.91	2.71		0.085	0.005	31.9
D11-4b*	10.01	10.43	1.00	0.76	0.6	2.91	2.68		0.087	0.007	30.7
D11-5*	10.80	10.05	2.00	4.44	4.8	5.35	4.42		0.204	0.005	21.7
D11-6*	12.43	10.63	4.00	4.84	5.8	9.20	-		0.208	0.009	-
D5 - Rhyodacite (850˚C)					$D^{fluid/melt}$ = 95±24						
D5-1	11.15	10.62	0.05	-		0.16	0.16		0.002	0.001	68.2
D5-2	10.58	9.81	0.10	-		0.32	0.31		0.004	0.001	80.7
D5-3	10.68	9.53	0.25	-		0.78	0.77		0.015	0.002	51.9
D5-4*	10.04	10.58	0.40	0.39	<0.5	1.23	1.14		0.010	0.001	113.7
D5-5*	10.17	10.18	0.50	0.30	<0.5	1.53	1.44	1.28	0.022	0.004	66.8
D5-6*	10.31	10.22	0.80	0.24	<0.5	2.38	2.31	1.24	0.020	0.009	114.1
D5-7*	11.36	10.95	1.00	0.95		2.92	2.71	1.37	0.026	0.005	104.8
D5-8*	10.71	11.02	1.25	1.00		3.57	3.34	1.62	0.032	0.005	104.9
RD11 - Rhyolite (900˚C)					$D^{fluid/melt}$ = 101±19						
RD11-7	9.45	10.12	0.05	-		0.16	0.16		0.002	0.001	67.6
RD11-1	10.04	11.96	0.10	-		0.32	0.31		0.003	0.001	94.2
RD11-2	11.30	11.17	0.25	-		0.78	0.78		0.006	0.001	129.8
RD11-8	10.13	10.13	0.40	-		1.23	1.22		0.014	0.002	87.9
RD11-3	9.98	10.81	0.50	-		1.53	1.51		0.016	0.002	97.1
RD11-4*	11.41	11.78	1.00	0.57	<0.5	2.91	2.78		0.027	0.003	104.1
RD11-5*	11.04	14.53	2.00	0.51	0.5	5.35	-		0.036	0.001	-
RD11-6*	13.48	12.07	4.00	0.40		9.20	-		0.047	0.004	-
RD12 - Rhyolite (800˚C)					$D^{fluid/melt}$ = 114±43						
RD12-5	11.19	10.12	0.05	-		0.16	0.16	0.14	0.005	0.001	33.4
RD12-1	9.82	9.77	0.10	-		0.32	0.31		0.005	0.002	56.8
RD12-2	9.96	9.46	0.25	-		0.78	0.77		0.011	0.002	67.4
RD12-6	11.36	10.46	0.40	-		1.23	1.22	0.74	0.014	0.004	89.9
RD12-3*	9.87	10.78	0.50	0.92		1.53	1.31		0.011	0.001	123.3
RD12-7*	10.50	10.10	0.80	1.22		2.38	2.13		0.018	0.003	117.2
RD12-4*	10.47	10.37	1.00	0.49		2.38	-		0.015	0.001	-
RD12-8*	10.92	10.51	1.25	1.12		3.57	3.34		0.027	0.005	125.1

* Anhydrite-saturated experiments

$Anhy^{1}$ = Amount of anhydrite determined by mass balance
$Anhy^{2}$ = Amount of anhydrite determined by image analyses
S^{bulk} = Bulk sulfur content in the H_2SO_4 solution added to the capsule
S^{fluid} = Amount of sulfur in the fluid determined by mass balance
S^{melt} = Amount of sulfur in the melt determined by microprobe
S^{fluid}_{Raman} = Amount of sulfur in the fluid determined by Raman spectroscopy using calibration from (Binder and Keppler, 2011)
$D_S^{fluid/melt}$ = Fluid/melt partition coefficient of sulfur

Table 3

Table 3. Major element compositions of experimental glasses.

Run (σ)[1]	SiO_2	TiO_2	Al_2O_3	FeO	MgO	CaO	Na_2O	K_2O	Total	S (ppm)	H_2O^-	$\ln K_{SP}^{anhy}$	$\ln K_{SP}^{anhy}$ (M&K2015)
A18 - Trachy-andesite (950˚C)													
A18-7	55.62	0.69	18.29	2.64	1.21	4.27	5.24	3.43	91.38	493	8.62		
(20)	0.15	0.05	0.08	0.06	0.03	0.07	0.08	0.04		200			
A18-1	56.75	0.60	18.85	1.84	1.18	4.17	5.45	3.55	92.39	1222	7.61		
(20)	0.29	0.06	0.19	0.05	0.05	0.15	0.10	0.08		299			
A18-2*	57.10	0.58	19.21	1.90	1.23	3.17	5.52	3.58	92.28	1525	7.72	-8.96	-8.28
(19)	0.24	0.10	0.35	0.14	0.05	0.08	0.19	0.09		50			
A18-8*	57.11	0.71	18.55	2.43	1.23	2.93	5.27	3.45	91.68	1689	8.34	-8.93	-8.46
(20)	0.25	0.04	0.10	0.05	0.04	0.12	0.08	0.06		34			
A18-3*	58.05	0.53	19.40	1.14	1.14	1.96	5.59	3.64	91.46	1795	8.54	-9.26	-8.85
(20)	0.27	0.04	0.18	0.07	0.07	0.12	0.13	0.08		67			
A18-4*	59.07	0.49	18.88	1.57	0.96	1.23	5.39	3.65	91.23	2059	8.77	-9.59	-9.23
(20)	0.16	0.03	0.17	0.05	0.03	0.06	0.12	0.09		42			
A18-5*	65.23	0.48	17.01	1.28	0.64	0.69	4.50	3.35	93.19	2434	6.81	-10.03	-9.65
(19)	0.33	0.05	0.20	0.06	0.07	0.07	0.16	0.10		87			
A18-6*	70.28	0.46	13.82	1.11	0.19	0.28	3.42	2.96	92.52	2701	7.48	-10.87	-9.88
(20)	0.18	0.07	0.12	0.04	0.02	0.04	0.12	0.10		62			
A13 – Trachyte (900˚C)													
A13-7	58.45	0.43	18.88	1.47	0.94	2.32	5.39	4.82	92.70	78	7.30		
(15)	0.11	0.04	0.11	0.05	0.03	0.06	0.06	0.04		14			
A13-1	58.77	0.41	18.98	1.50	0.73	2.34	5.46	4.77	92.96	230	7.04		
(20)	0.30	0.05	0.13	0.09	0.04	0.09	0.33	0.08		27			
A13-2	58.78	0.38	18.87	1.48	0.73	2.27	5.52	4.75	92.77	482	7.23		
(20)	0.23	0.04	0.14	0.06	0.05	0.09	0.16	0.11		24			
A13-8	58.42	0.41	18.71	1.49	0.93	2.29	5.41	4.79	92.45	661	7.55		
(15)	0.14	0.03	0.13	0.05	0.03	0.04	0.08	0.04		19			
A13-3*	58.97	0.39	18.70	1.50	0.73	1.98	5.38	4.76	92.40	1118	7.60	-9.73	-10.02
(20)	0.21	0.04	0.16	0.05	0.03	0.08	0.10	0.11		56			
A13-3b*	59.40	0.37	18.83	1.41	0.69	2.04	5.58	4.71	93.04	879	6.96	-9.94	-10.28
(15)	0.12	0.03	0.08	0.03	0.02	0.04	0.10	0.06		83			
A13-4*	59.14	0.43	18.81	1.49	0.77	1.41	5.40	4.80	92.26	1214	7.74	-9.98	-10.27
(20)	0.28	0.05	0.19	0.06	0.05	0.06	0.12	0.08		219			

A13-5*	58.71	0.43	18.93	1.43	0.79	1.23	5.38	4.81	91.71	1531	8.29	-9.88	-10.20
(20)	0.43	0.05	0.32	0.06	0.05	0.06	0.15	0.10		32			
A13-6*	60.31	0.45	18.75	1.26	0.67	0.89	5.16	4.78	92.27	1742	7.73	-10.08	-10.86
(20)	0.28	0.05	0.22	0.04	0.05	0.04	0.14	0.11		50			
A15 – Trachyte (850˚C)													
A15-1	63.42	0.33	16.00	1.38	0.15	1.08	4.99	6.25	93.59	144	6.41		
(15)	0.18	0.05	0.12	0.05	0.01	0.04	0.08	0.08		56			
A15-2	63.89	0.34	16.13	1.37	0.17	0.97	5.12	6.31	94.29	416	5.71		
(15)	0.16	0.04	0.07	0.04	0.02	0.04	0.10	0.06		13			
A15-3*	64.44	0.41	15.95	1.43	0.21	0.87	5.06	6.29	94.67	431	5.33	-11.54	-11.51
(15)	0.14	0.03	0.14	0.04	0.02	0.04	0.07	0.10		18			
A15-4*	63.95	0.44	16.16	1.20	0.19	0.57	4.91	6.23	93.65	602	6.35	-11.61	-11.68
(15)	0.46	0.04	0.36	0.06	0.02	0.05	0.14	0.08		22			
A15-5*	62.83	0.44	15.92	1.28	0.22	0.54	4.64	6.25	92.11	641	7.89	-11.58	-11.06
(20)	0.15	0.04	0.12	0.04	0.02	0.03	0.10	0.09		27			
A15-6*	63.58	0.43	15.97	1.17	0.20	0.43	4.52	6.17	92.48	716	7.52	-11.71	-11.52
(15)	0.42	0.04	0.31	0.03	0.02	0.04	0.14	0.11		19			
A15-7*	63.23	0.40	15.99	1.09	0.19	0.38	4.52	6.18	91.98	775	8.02	-11.76	-11.42
(20)	0.85	0.03	0.64	0.04	0.02	0.04	0.17	0.08		54			
A15-8*	63.03	0.40	16.58	1.05	0.21	0.42	4.61	6.06	92.36	906	7.64	-11.49	-11.79
(15)	0.99	0.03	0.64	0.05	0.03	0.08	0.20	0.08		43			
D11 – Dacite (900˚C)													
D11-7	61.78	0.62	17.43	2.01	1.34	2.19	4.88	2.10	92.35	42	7.65		
(15)	0.14	0.03	0.11	0.04	0.03	0.05	0.10	0.03		9			
D11-1	60.73	0.48	17.46	1.50	1.31	2.19	5.05	2.10	90.82	502	9.18		
(20)	0.32	0.06	0.23	0.10	0.07	0.08	0.12	0.05		37			
D11-2	61.31	0.65	17.43	2.01	1.30	2.00	5.07	2.11	91.87	756	8.13		
(20)	0.32	0.05	0.18	0.07	0.05	0.08	0.12	0.06		112			
D11-8*	61.77	0.59	17.25	1.98	1.33	2.09	4.92	2.11	92.04	882	7.96	-9.95	-9.82
(15)	0.18	0.04	0.14	0.07	0.04	0.05	0.06	0.04		18			
D11-3	61.03	0.64	17.40	2.01	1.31	2.19	5.03	2.08	91.69	723	8.31		
(20)	0.32	0.05	0.24	0.05	0.06	0.08	0.12	0.07		58			
D11-4*	61.27	0.46	17.48	1.47	1.30	2.02	5.01	2.09	91.10	851	8.90	-10.01	-9.75
(20)	0.26	0.08	0.21	0.13	0.06	0.07	0.11	0.06		47			
D11-4b*	62.56	0.60	17.29	1.94	1.35	2.05	5.04	2.07	92.90	873	7.10	-9.99	-10.17

(15)	0.23	0.03	0.13	0.06	0.02	0.08	0.08	0.04		68			
D11-5*	63.06	0.44	17.07	1.45	1.02	0.63	4.84	2.10	90.62	2038	9.38	-10.28	-10.51
(20)	0.33	0.05	0.21	0.07	0.05	0.05	0.18	0.07		52			
D11-6*	64.75	0.41	16.15	1.55	0.84	0.49	4.43	2.04	90.66	2080	9.34	-10.54	-10.65
(20)	0.54	0.04	0.36	0.07	0.06	0.04	0.26	0.08		86			
D5 – Rhyodacite (850˚C)													
D5-1	67.14	0.32	16.09	1.47	0.54	1.44	4.15	2.55	93.71	23	6.29		
(15)	0.17	0.02	0.08	0.04	0.02	0.05	0.09	0.04		6			
D5-2	67.21	0.33	16.10	1.14	0.34	1.45	4.17	2.40	93.13	39	6.87		
(15)	0.14	0.04	0.08	0.09	0.04	0.04	0.08	0.06		9			
D5-3	66.83	0.31	16.06	0.88	0.22	1.48	3.98	2.35	92.10	148	7.90		
(15)	0.22	0.02	0.10	0.07	0.04	0.05	0.15	0.08		20			
D5-4*	67.33	0.31	15.98	1.45	0.55	1.44	4.17	2.52	93.76	100	6.24	-12.52	-12.63
(15)	0.15	0.03	0.09	0.05	0.03	0.04	0.08	0.06		12			
D5-5*	65.91	0.32	16.05	1.53	0.54	1.46	4.04	2.53	92.37	216	7.63	-11.72	-12.13
(15)	0.20	0.03	0.14	0.05	0.02	0.04	0.06	0.06		44			
D5-6*	65.92	0.33	16.19	1.49	0.48	1.48	4.06	2.52	92.48	203	7.52	-11.77	-12.28
(15)	0.14	0.03	0.13	0.07	0.02	0.05	0.05	0.04		87			
D5-7*	65.67	0.32	16.19	1.53	0.52	1.21	4.11	2.53	92.09	259	7.91	-11.49	-12.00
(20)	0.58	0.03	0.40	0.05	0.05	0.14	0.11	0.07		54			
D5-8*	65.91	0.32	16.07	1.54	0.56	1.19	4.04	2.49	92.13	318	7.87	-11.25	-11.93
(20)	0.52	0.04	0.26	0.08	0.06	0.20	0.17	0.07		50			
RD11 – Rhyolite (900˚C)													
RD11-7	68.33	0.55	14.24	1.17	0.36	1.81	3.50	3.46	93.42	23	6.58		
(15)	0.19	0.04	0.10	0.03	0.02	0.06	0.08	0.04		12			
RD11-1	66.41	0.53	14.28	1.19	0.35	1.77	3.51	3.45	91.49	33	8.51		
(20)	0.24	0.06	0.21	0.06	0.02	0.06	0.08	0.09		14			
RD11-2	66.56	0.52	14.35	1.21	0.34	1.79	3.51	3.48	91.75	60	8.25		
(20)	0.23	0.05	0.18	0.05	0.03	0.07	0.10	0.07		13			
RD11-8	68.46	0.54	14.27	1.19	0.36	1.82	3.51	3.46	93.61	139	6.39		
(15)	0.16	0.03	0.08	0.03	0.03	0.06	0.06	0.05		19			
RD11-3	64.57	0.53	13.96	0.61	0.06	1.74	2.78	3.16	87.41	156	12.59		
(20)	0.45	0.07	0.20	0.09	0.03	0.17	0.35	0.20		18			
RD11-4*	65.63	0.52	13.91	0.68	0.10	1.74	2.58	3.10	88.25	267	11.75	-11.30	-9.83
(20)	0.50	0.06	0.13	0.19	0.07	0.15	0.36	0.25		28			

RD11-5*	67.21	0.54	14.25	1.23	0.32	1.59	3.45	3.49	92.08	356	7.92	-11.14	-10.60
(20)	0.20	0.05	0.18	0.06	0.03	0.09	0.09	0.11		14			
RD11-6*	67.23	0.55	14.44	1.22	0.30	1.16	3.49	3.52	91.91	468	8.09	-11.17	-10.81
(20)	0.44	0.07	0.25	0.05	0.03	0.08	0.09	0.08		40			
RD12 – Rhyolite (800˚C)													
RD12-5	70.35	0.19	12.47	0.88	0.25	1.04	2.86	4.34	92.38	46	7.62		
(20)	0.26	0.02	0.17	0.05	0.03	0.05	0.06	0.06		12			
RD12-1	69.51	0.22	12.67	0.92	0.25	0.99	2.85	4.40	91.81	55	8.19		
(20)	0.28	0.04	0.18	0.05	0.03	0.06	0.07	0.11		21			
RD12-2	71.11	0.18	12.51	0.75	0.22	0.51	2.82	4.39	92.49	114	7.51		
(20)	0.59	0.05	0.38	0.06	0.04	0.08	0.12	0.10		16			
RD12-6	70.70	0.19	12.52	0.87	0.25	0.64	2.80	4.38	92.36	136	7.64		
(20)	0.50	0.02	0.32	0.05	0.02	0.08	0.10	0.07		36			
RD12-3*	70.87	0.17	12.69	0.75	0.25	0.64	2.83	4.45	92.65	106	7.35	-13.27	-13.34
(15)	0.50	0.04	0.18	0.05	0.03	0.06	0.35	0.21		8			
RD12-7*	69.94	0.22	12.33	0.76	0.22	0.51	1.90	3.88	89.76	181	10.24	-12.93	-13.25
(20)	0.66	0.03	0.17	0.13	0.04	0.10	0.42	0.51		31			
RD12-4*	70.17	0.21	12.72	0.90	0.25	0.80	2.83	4.39	92.28	146	7.72	-12.72	-12.98
(15)	0.18	0.03	0.09	0.03	0.02	0.04	0.09	0.13		13			
RD12-8*	69.32	0.21	12.71	0.87	0.25	0.55	1.94	3.99	89.84	267	10.16	-12.48	-13.23
(20)	0.47	0.03	0.20	0.07	0.03	0.09	0.24	0.28		50			

* Anhydrite-saturated experiments

[1]σ = standard deviation, the number of analyses is reported in parenthesis

H_2O^- = amount of water in the melt, determined using the "by difference" technique (Devine et al., 1995)

ln K_{SP}^{anhy} = Solubility product of anhydrite, calculated in molar fraction [$K_{SP}^{anhy} = X_{CaO} * X_{SO3}$]

ln K_{SP}^{anhy} (M&K2015) = Solubility product of anhydrite, predicted by the model proposed by (Masotta and Keppler, 2015)

Figure 1

Click here to download high resolution image

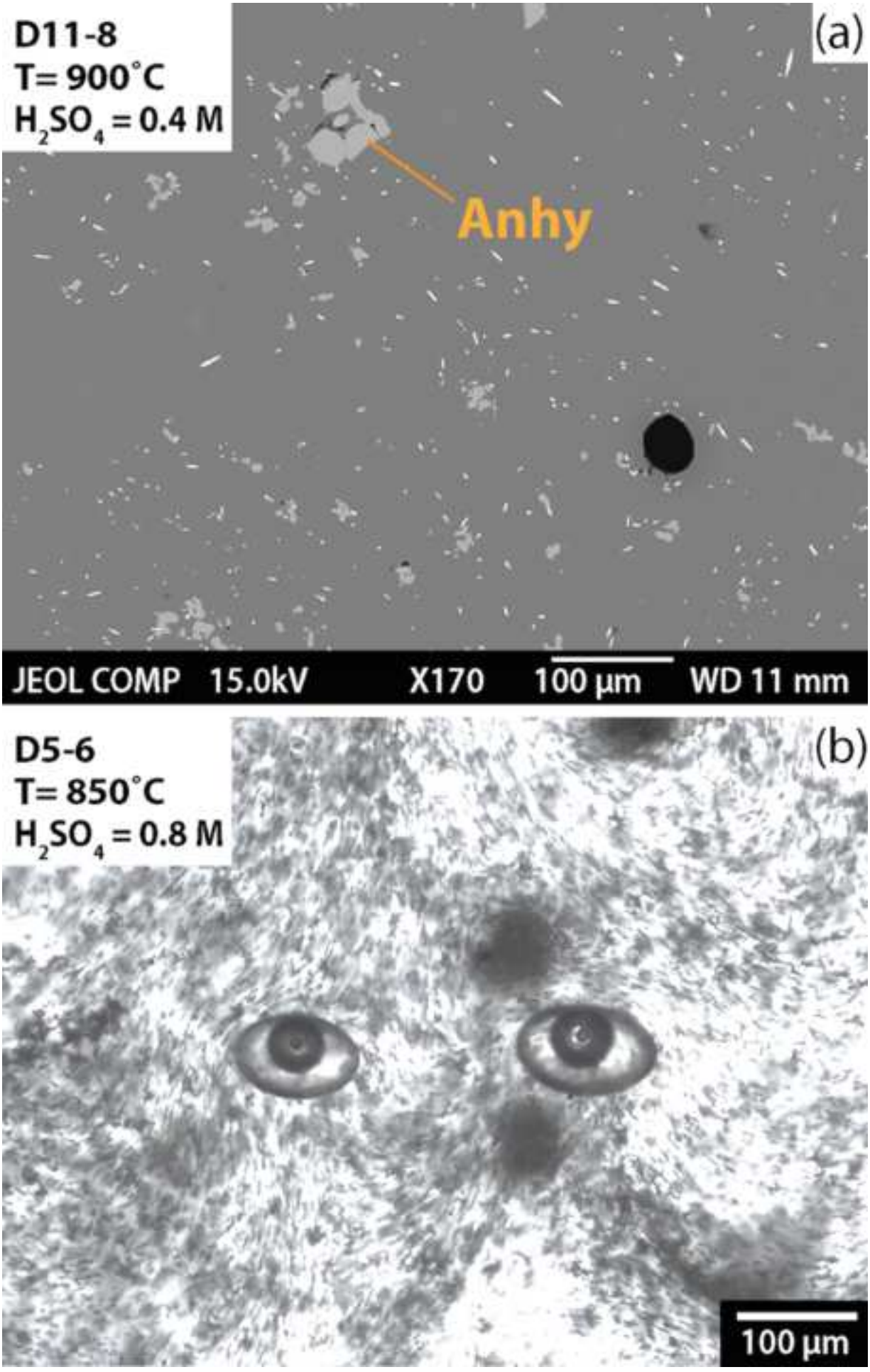

Figure 2

Click here to download high resolution image

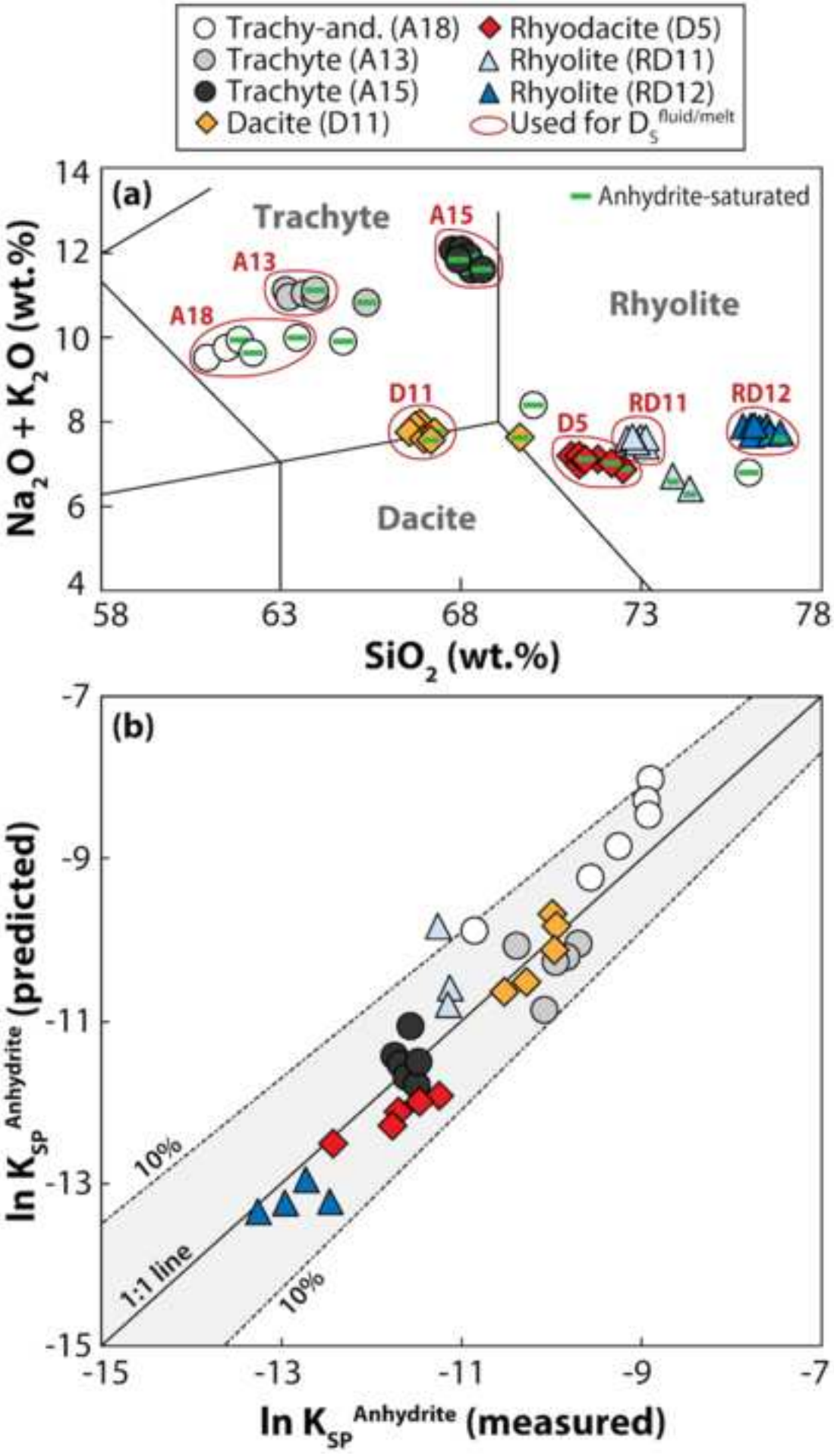

Figure 3

Click here to download high resolution image

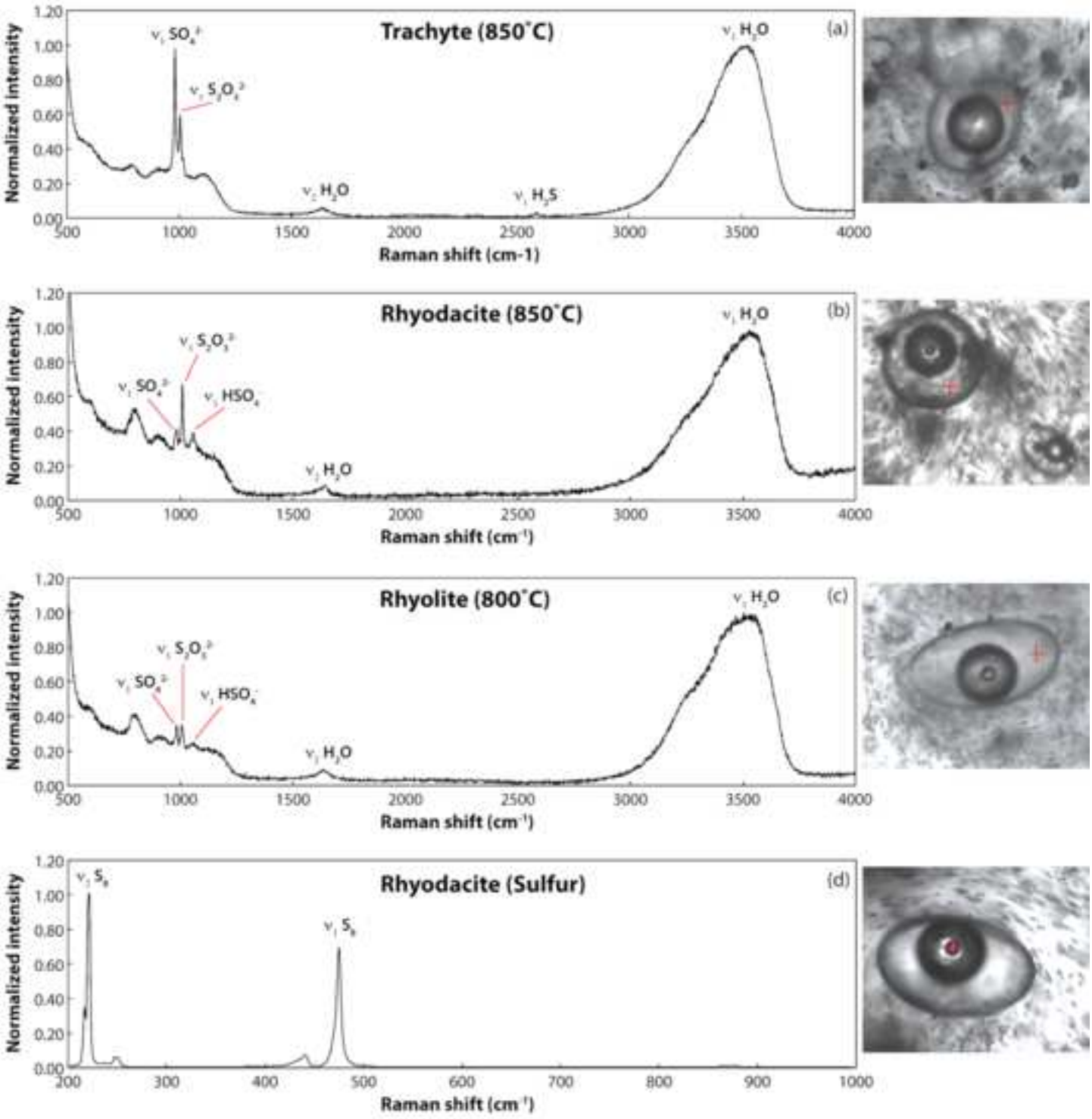

Figure 4
Click here to download high resolution image

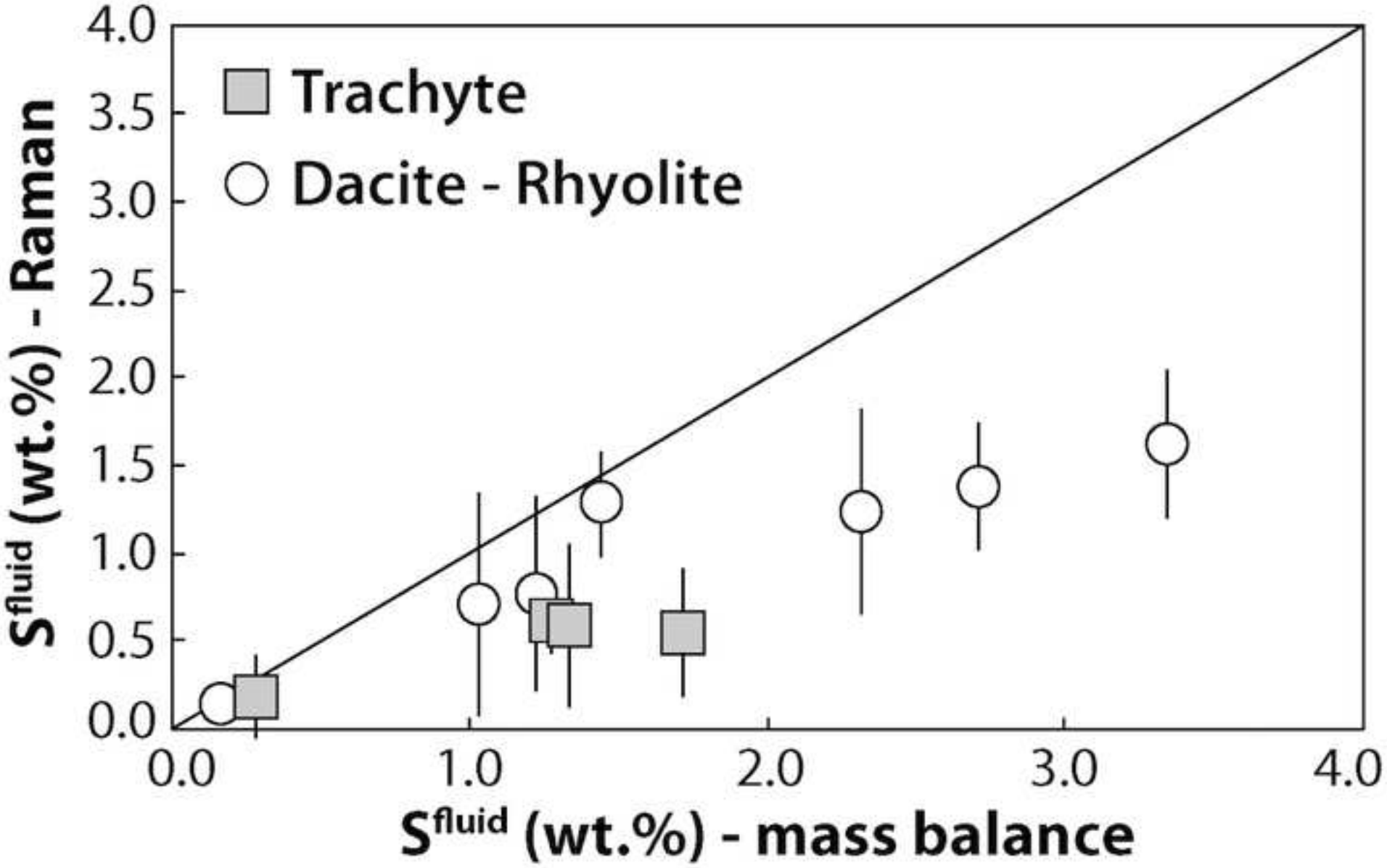

Figure 5
Click here to download high resolution image

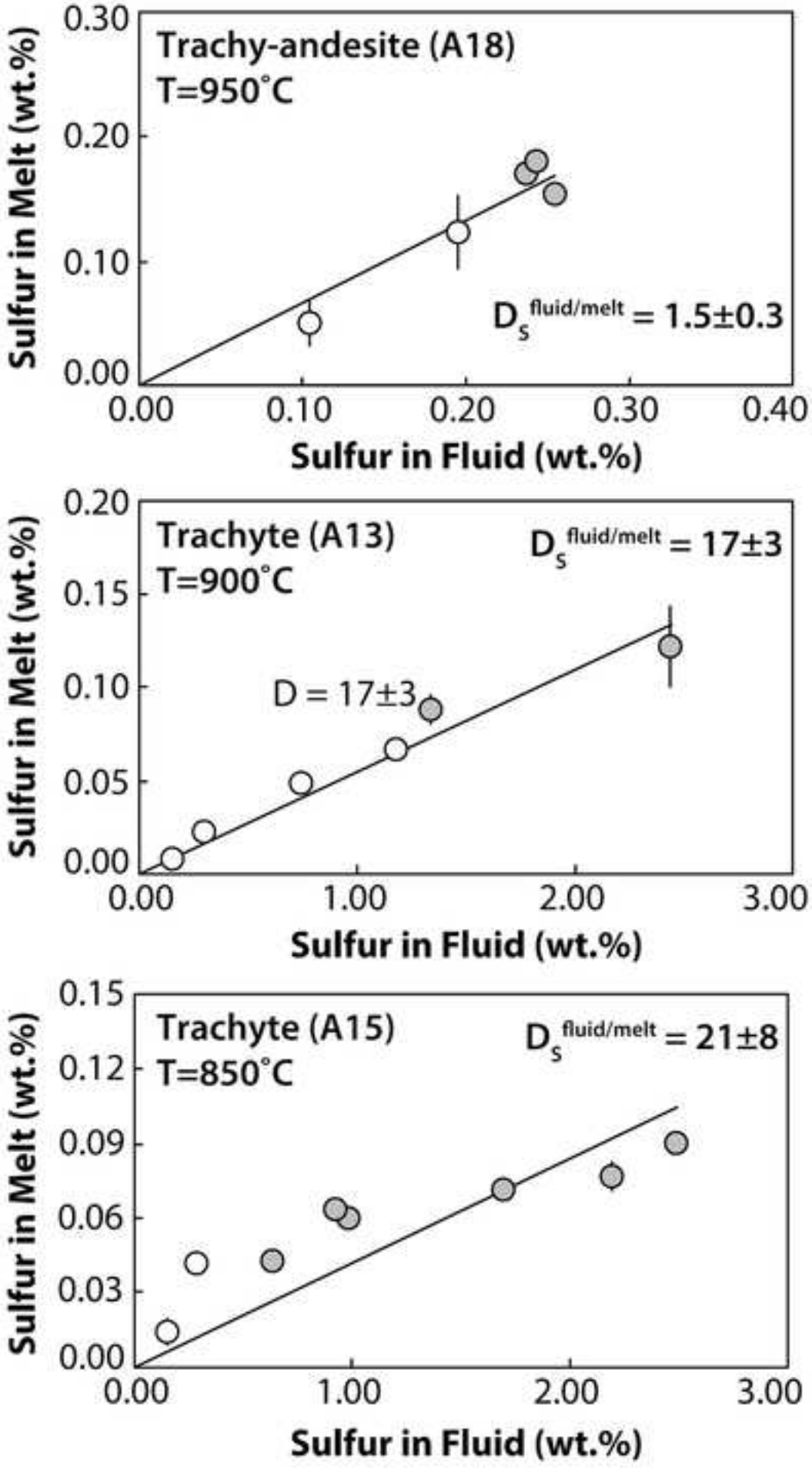

Figure 6
Click here to download high resolution image

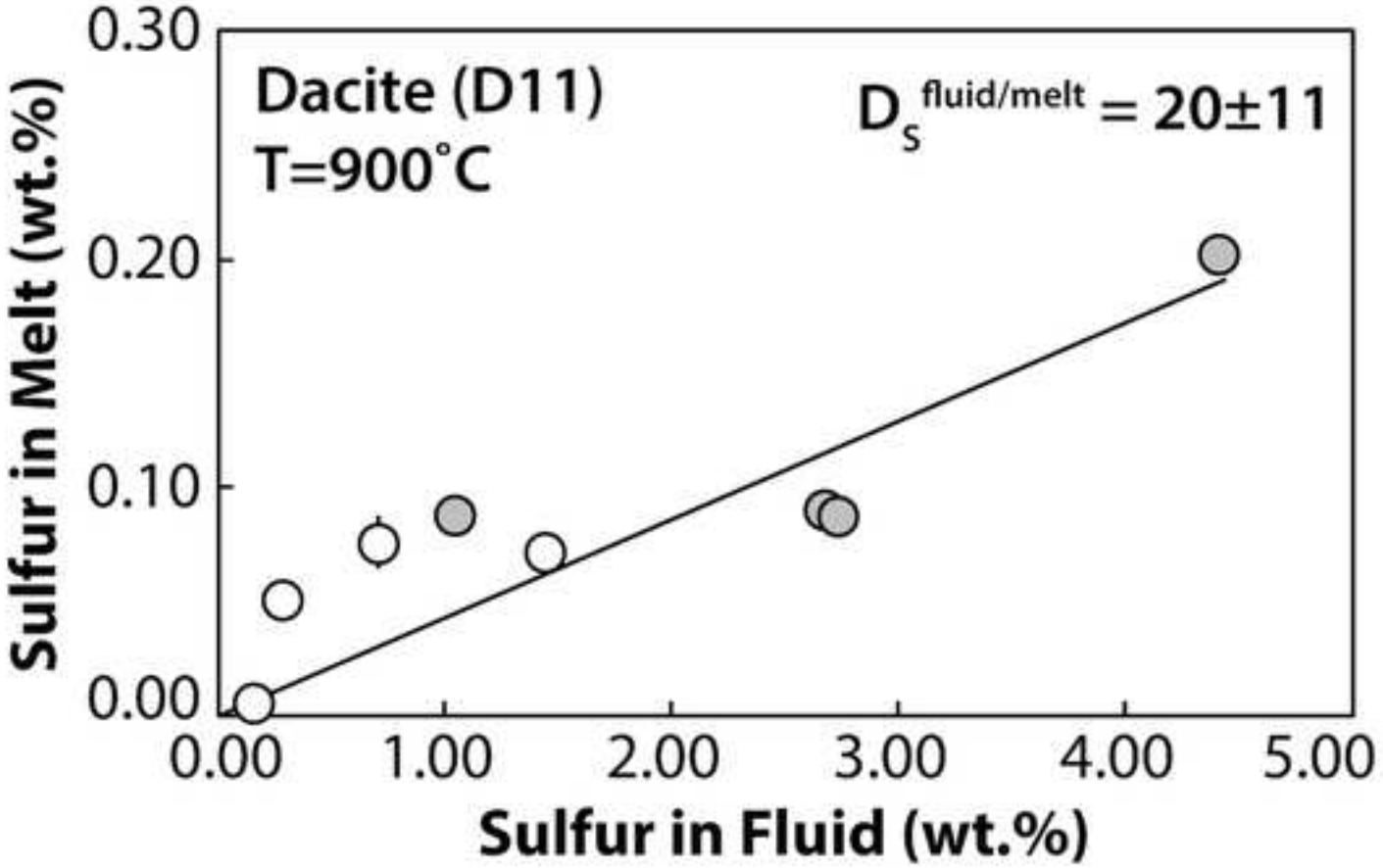

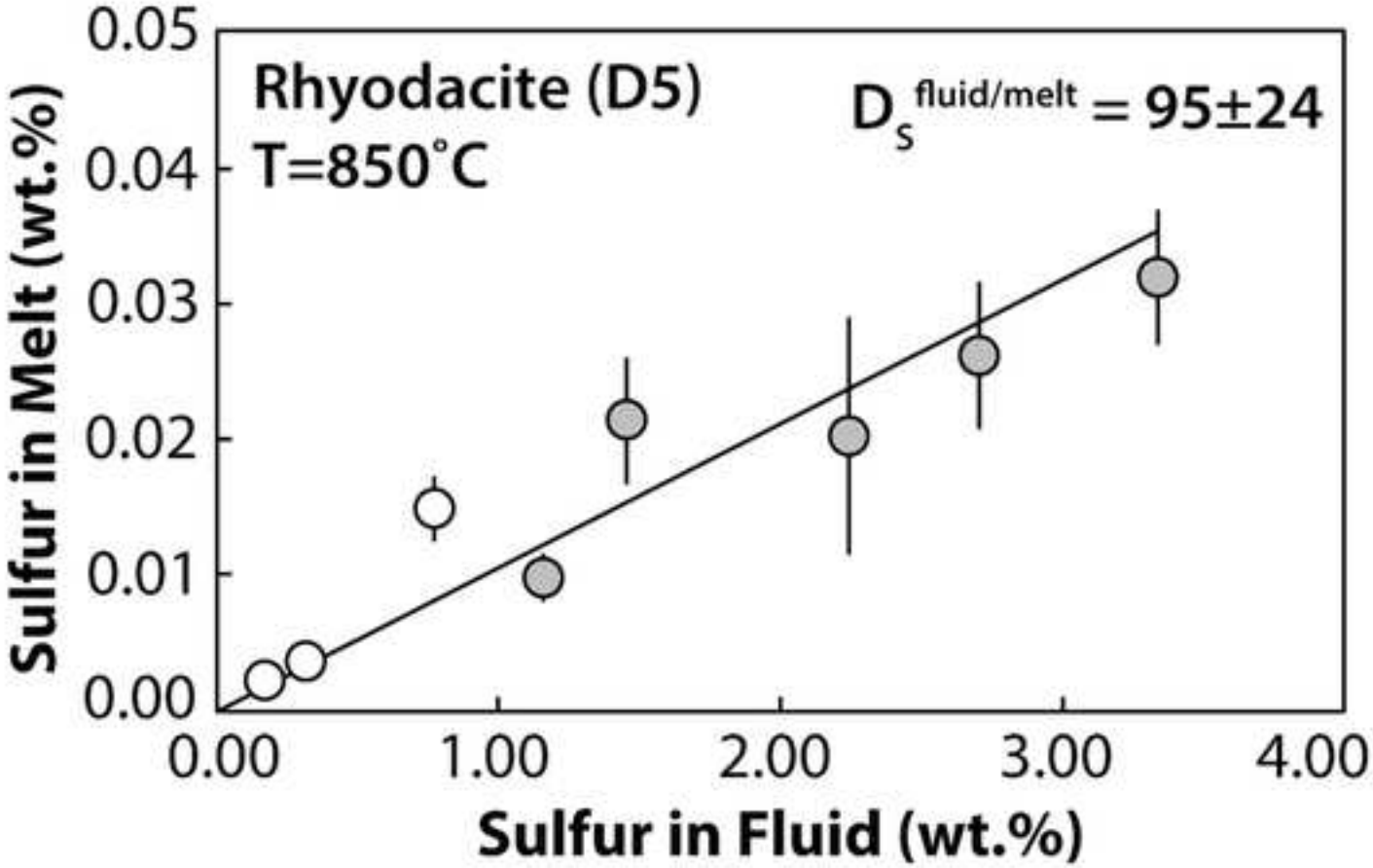

Figure 7
Click here to download high resolution image

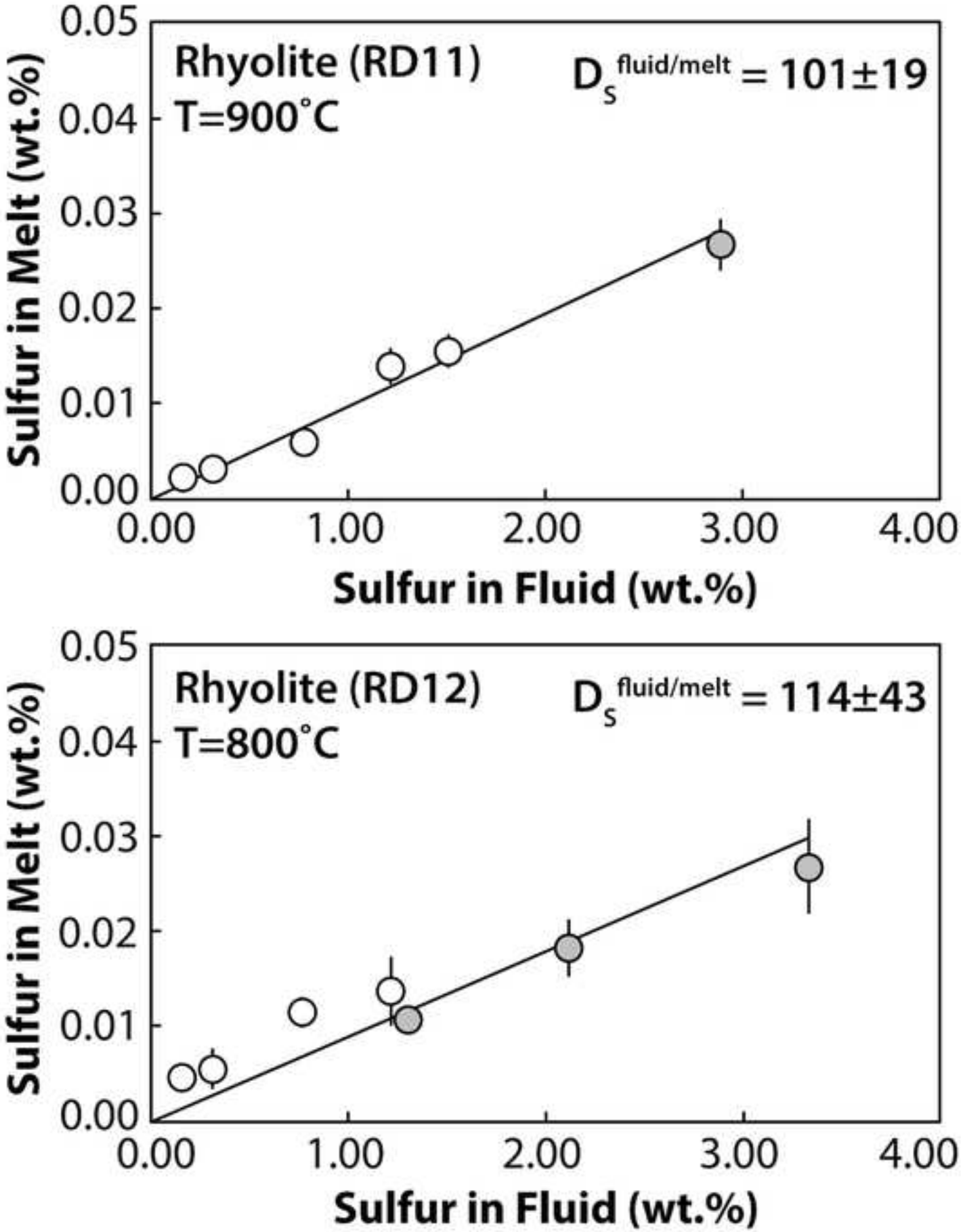

Figure 8

Click here to download high resolution image

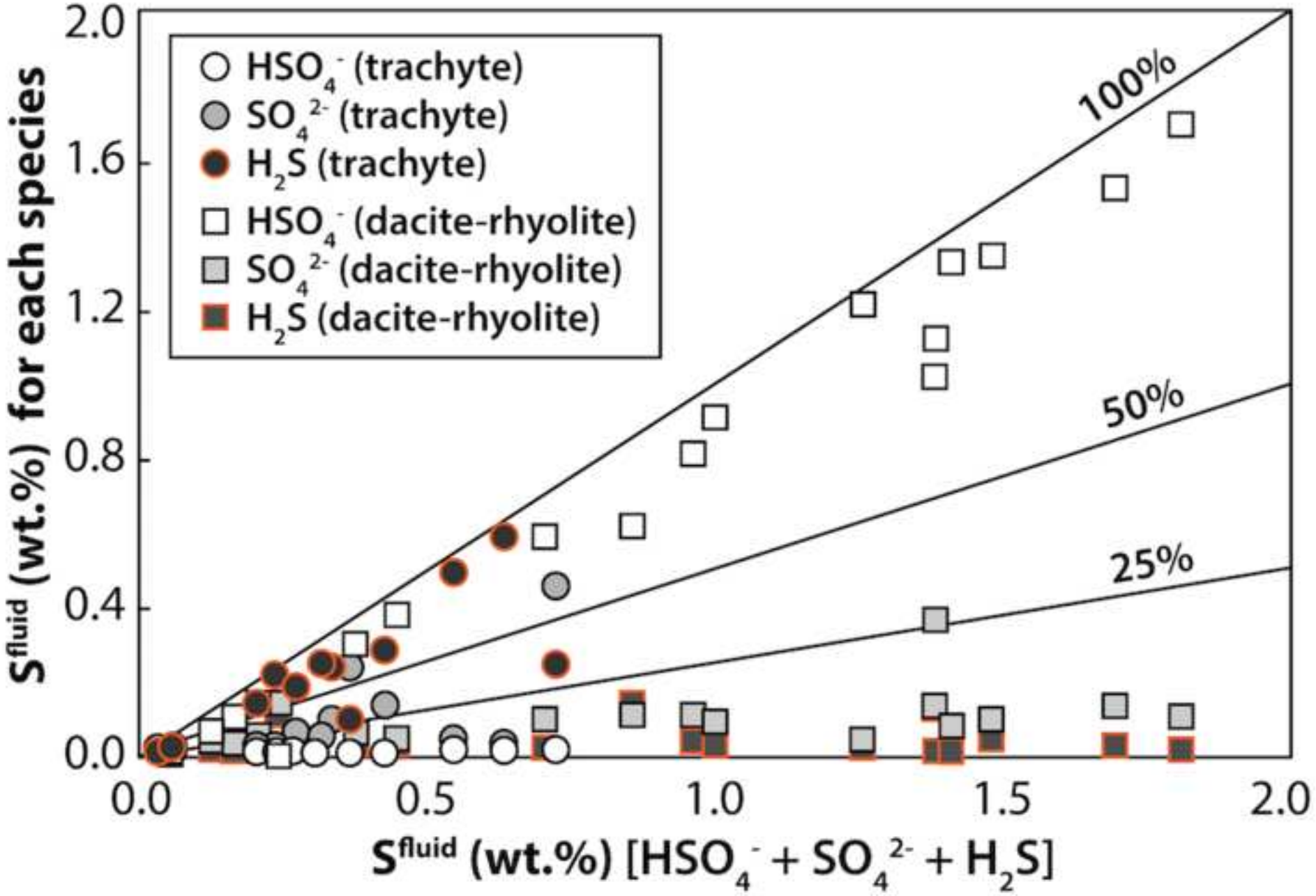

Figure 9
Click here to download high resolution image

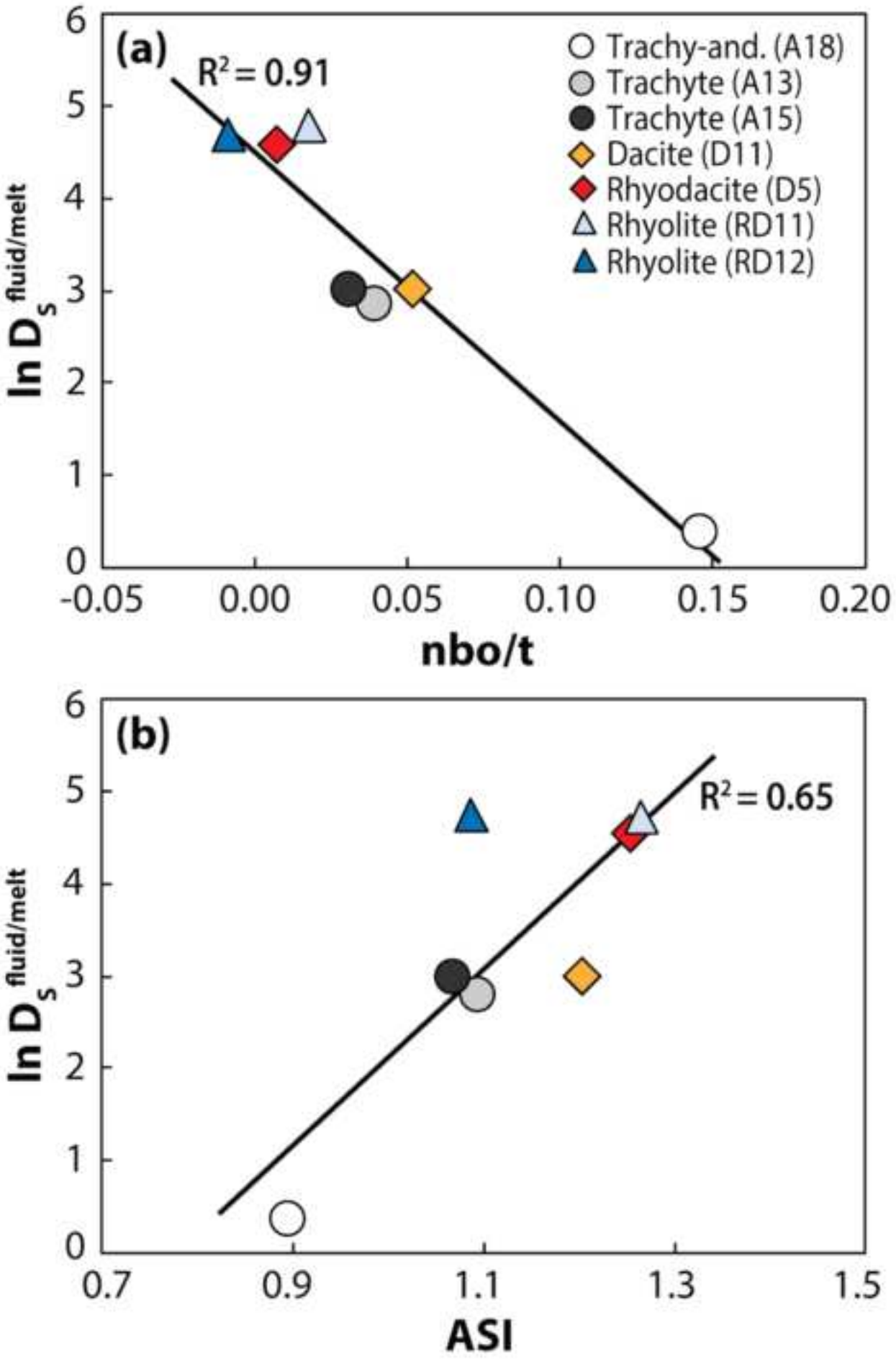

Figure 10
Click here to download high resolution image

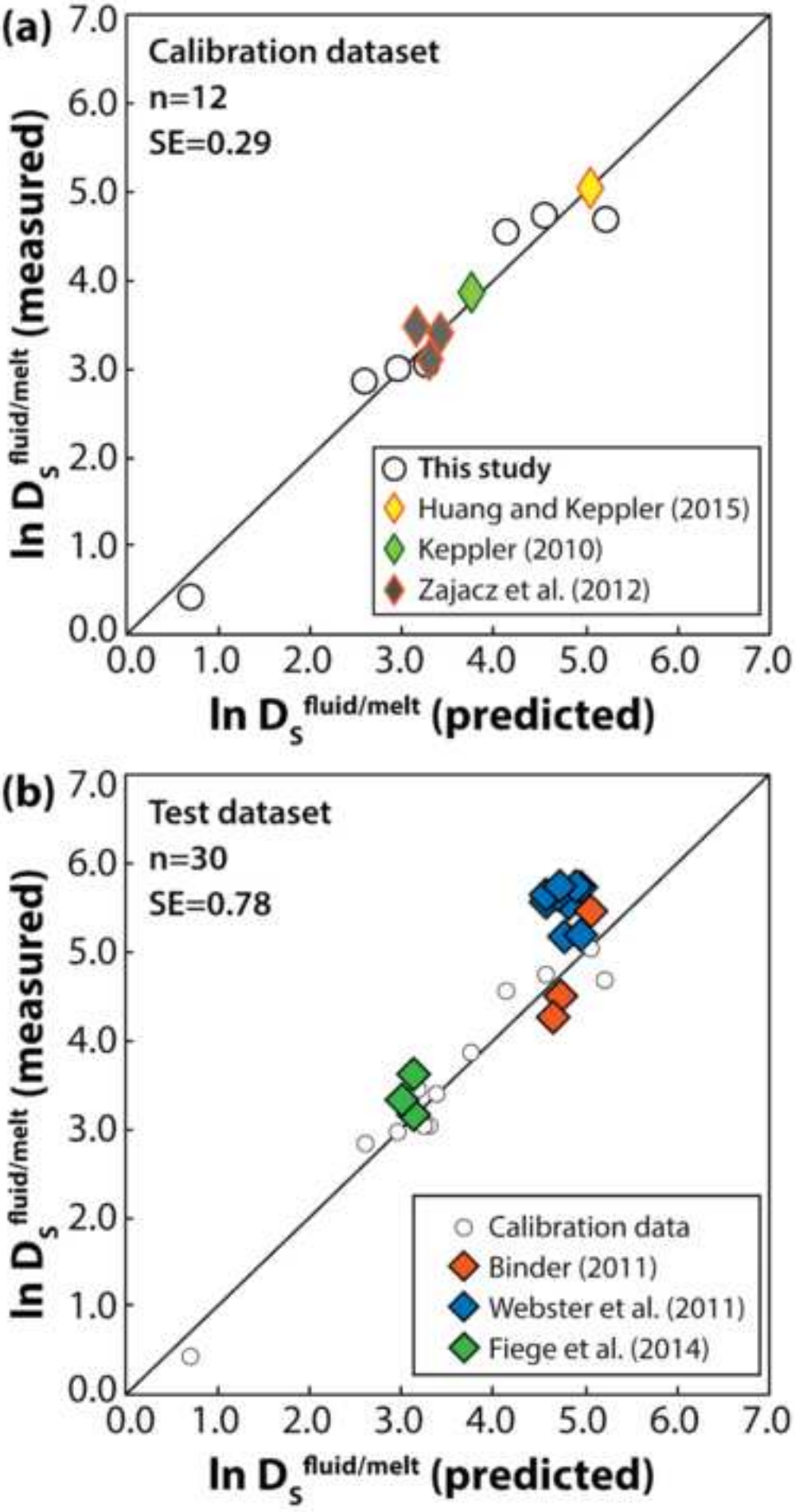

Figure 11
Click here to download high resolution image

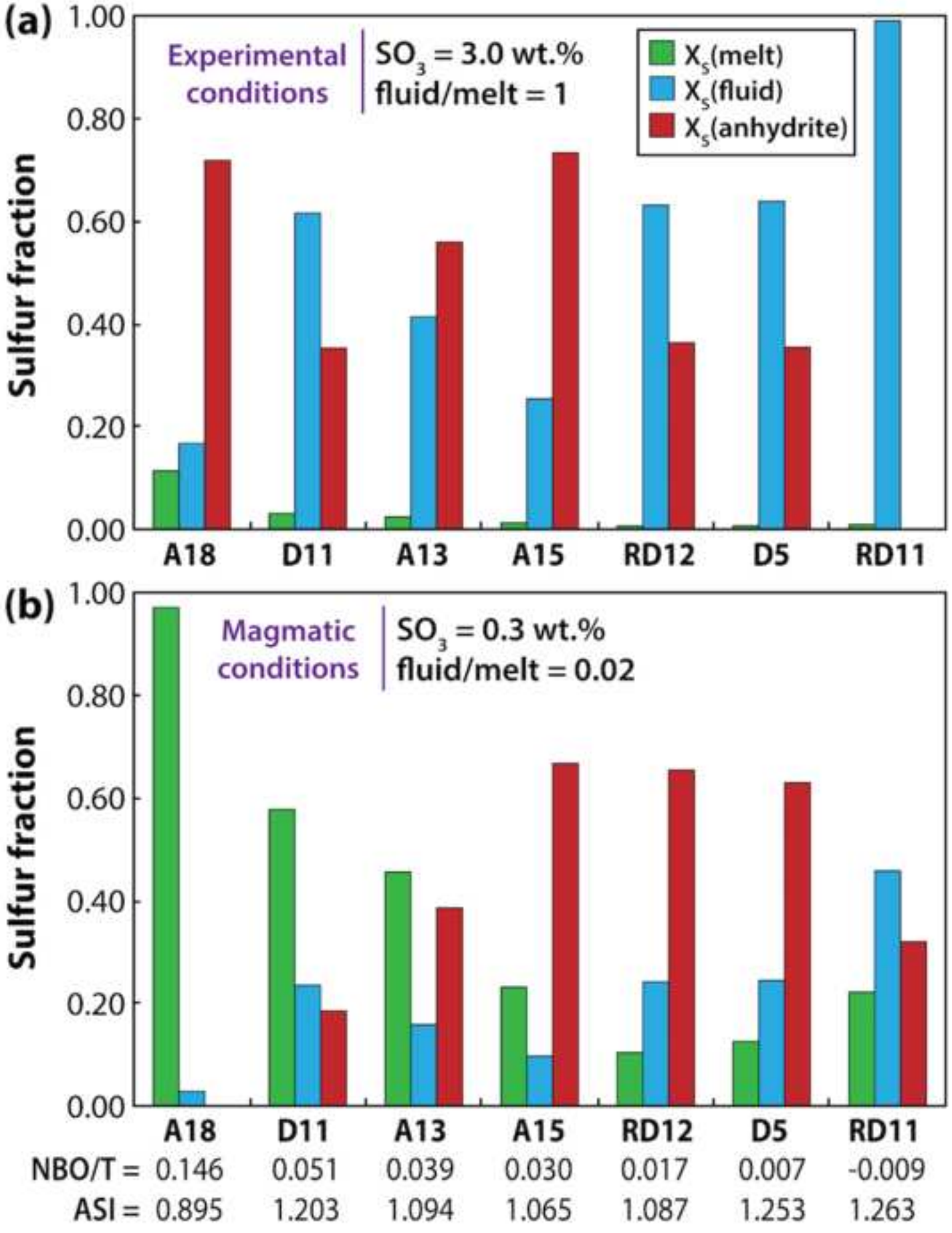

Figure 12

Click here to download high resolution image

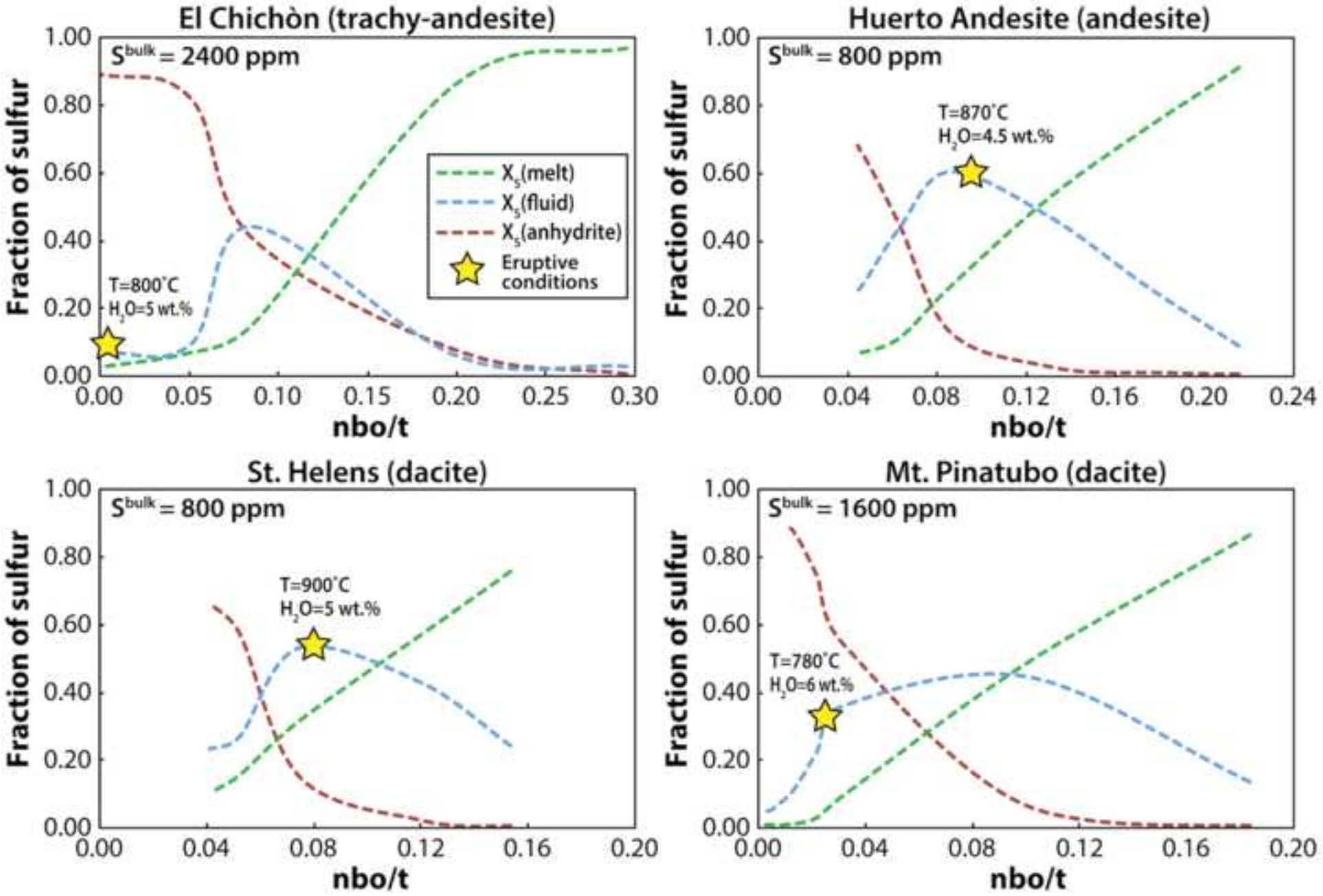

Figure 13

Click here to download high resolution image